Emergence and equilibration of jets in beta-plane turbulence

NAVID C. CONSTANTINOU[1], PETROS J. IOANNOU[1]† AND BRIAN F. FARRELL[2]

[1]Department of Physics, National and Kapodistrian University of Athens, Panepistimiopolis,
15784 Athens, Greece

[2]Department of Earth and Planetary Sciences, Harvard University, Geological Museum 452, 24
Oxford Street, Cambridge, MA 02138, USA

(Received ?; revised ?; accepted ?.)

Coherent large scale jets that are not forced directly at the jet scale are a prominent feature of rotating turbulence. These jets arise and are supported by systematic organization of the turbulent Reynolds stresses. Understanding the mechanism producing the required eddy momentum flux convergence, and how the jets and associated eddy field mutually adjust to maintain a steady jet structure at finite amplitude, constitute fundamental theoretical problems. Stochastic Structural Stability Theory (SSST) provides a framework for understanding the emergence and equilibration of jets based on a statistical mean state dynamics of turbulence that is closed at second order. SSST reveals a new manifold of turbulent equilibria and linearization of the SSST dynamics about these equilibria allows formulation of a structural stability theory that predicts the emergence of jets from homogeneous turbulence. In this work we test predictions of this statistical mean state dynamics for both formation and equilibration of turbulent jets using quasi-linear and nonlinear simulations of barotropic turbulence on a beta-plane. We find that SSST accurately predicts both the initial emergence and the finite amplitude equilibration of jets in beta-plane turbulence.

Key words: Atmospheric flows, Wave-turbulence interactions, Instability

1. Introduction

Spatially and temporally coherent jets are a common feature of turbulent flows in planetary atmospheres with the banded winds of the giant planets constituting a familiar example (Vasavada & Showman 2005). Fjörtöft (1953) noted that the essentially two dimensional large scale turbulence in planetary atmospheres, which results from the constraints of rapid rotation and strong stratification, would tend, given approximate conservation of energy and vorticity, to transfer turbulent energy to the largest scale available. This argument provides a conceptual basis for understanding the observed tendency for formation of large scale structure from small scale turbulence in planetary atmospheres. However, the observed large scale structure primarily takes the specific form of zonal jets and, moreover, the scale of these jets is distinct from the largest scale in the flow. Rhines (1975) argued that the observed jet scale results from the arrest of the inverse cascade at the length scale, $\sqrt{u/\beta}$, where $\beta = \mathrm{d}f/\mathrm{d}y$ is the meridional gradient of planetary vorticity and u is the root mean square velocity in the turbulent fluid.

---

† Email address for correspondence: pjioannou@phys.uoa.gr

In Rhines' interpretation this scale is identified with the scale at which the turbulent cascade is intercepted by the formation of propagating Rossby waves. More recently, it was proposed that jets in beta-plane turbulence arise from the tendency of turbulence to mix potential vorticity so that it becomes homogenized in limited regions forming potential vorticity staircases. The risers of these staircases correspond to thin prograde jets located at the latitudes of steep potential vorticity gradients separating parabolic retrograde jets corresponding to the well mixed steps of the staircase (Baldwin *et al.* 2007; Dritchel & McIntyre 2008). Another explanation for jet emergence has been advanced by Miller (1990) and Robert & Sommeria (1991). They associate formation of large scale jets with the tendency of two dimensional turbulent flows to form structures of maximum entropy while respecting energy and vorticity conservation. These statistical mechanical considerations predict the most likely structures to be zonal jets (Bouchet & Venaille 2012). Emergence of large scale structure in planetary flows has also been related to the existence of fixed points of the nonlinear planetary scale flow dynamics. Fixed point solutions were initially advanced to explain large scale persistent phenomena in the atmosphere such as blocking (Charney & DeVore 1979; Legras & Ghil 1985). These fixed point structures are solutions to the large scale laminar flow dynamics and do not include the influence on the dynamics of the interaction between the large scale structure and the smaller scale turbulence. Yet another proposed explanation for jet formation is modulational instability in which a zonal flow arises from nonlinear interaction of discrete Rossby waves (Gill 1974; Connaughton *et al.* 2010).

SSST provides an alternative explanation for jet formation that is fundamentally based on the interaction between jets and their associated field of turbulent eddies (Farrell & Ioannou 2003). In this theory, jets initially arise from a linear instability of this interaction and finite amplitude jets are identified as the nonlinear extension of these instabilities. SSST combines the full dynamics of the zonal mean flow with the second order statistics of the turbulent field obtained from a stochastic turbulence model (STM). The STM has been shown to provide accurate eddy statistics for the midlatitude atmosphere (Farrell & Ioannou 1993, 1994, 1995; Zhang & Held 1999; O'Gorman & Schneider 2007). These coupled equations determine the evolution of the mean zonal flow under the influence of its consistent field of eddies. The SSST equations predict jet formation from instabilities of the stationary solutions of this coupled dynamics and the instability of the stationary solutions as a function of parameters determines the bifurcation structure of the jet formation process. Srinivasan & Young (2012) developed a continuous formulation of SSST and used it to obtain analytic expressions for the emerging SSST instability in homogeneous beta-plane turbulence. A related quasi-linear approach to understanding finite amplitude turbulent equilibria in planetary atmospheres is the second order cumulant truncation method (CE2) (Marston *et al.* 2008; Marston 2012).

The quasi-linear (QL) approximation to the full nonlinear dynamics (NL) results when the perturbation-perturbation interactions are parameterized in the perturbation equations while interaction between the perturbations and the zonal mean flow is retained fully in the zonal mean equation. The SSST is based on QL with the additional assumption that the perturbation dynamics is that of the STM, which is equivalent to an infinite ensemble of perturbations evolving under QL. Because the SSST equations provide an autonomous and fluctuation-free dynamics of the statistical mean turbulent state, these equations facilitate analytic study of turbulent equilibria and their stability.

Previous studies demonstrated that unstable jets maintained by mean flow forcing can be equilibrated accurately using QL dynamics (Schoeberl & Lindzen 1984; DelSole & Farrell 1996; Marston *et al.* 2008). In contrast to these studies, in this work we investigate the emergence and equilibration of jets from homogeneous turbulence without coherent external forcing. SSST predicts that infinitesimal perturbations with zonal jet form organize homogeneous turbulence to produce systematic upgradient fluxes giving rise to exponential jet growth and eventually to the establishment of finite amplitude equilibrium jets. Specifically, the SSST equations predict initial formation of jets by the most unstable eigenmode of the linearized SSST dynamics. The formation of zonal jets from initially homogeneous beta-plane turbulence was studied with the methods of SSST by Farrell & Ioannou (2007); Bakas & Ioannou (2011, 2012) and by Srinivasan & Young (2012). In agreement with SSST, Srinivasan & Young (2012) found that NL simulations exhibit jet emergence from a homogeneous turbulent state with subsequent establishment of finite amplitude jets. In this paper we use the dynamics of the full NL equations and their QL approximation to examine further the mechanism of emergence and equilibration of jets from turbulence, concentrating on the effects of perturbation-perturbation nonlinearity on jet bifurcation and equilibration and on the influence of perturbations in exciting the manifold of SSST modes with jet structure.

2. Formulation of nonlinear barotropic dynamics on a beta-plane

Consider a beta-plane with x and y Cartesian coordinates along the zonal and the meridional direction respectively. The nondivergent zonal and meridional velocity fields are expressed in terms of a streamfunction, ψ, as $u = -\partial_y \psi$ and $v = \partial_x \psi$. The vorticity on the beta-plane is $q + 2\Omega + \beta y$, where $q \equiv \partial_x v - \partial_y u$ is the relative vorticity and $2\Omega + \beta y$ is the planetary vorticity. NL is governed by the beta-plane barotropic vorticity equation:

$$\partial_t q + u \partial_x q + v \partial_y q + \beta v = \sqrt{f} F - r q - \nu_4 \Delta^2 q \ . \tag{2.1}$$

The flow is dissipated with linear damping at rate r and hyperviscosity with coefficient ν_4. Periodic boundary conditions are imposed on x and y with periodicity $2\pi L$. In the above equation, distances have been nondimensionalized by a chosen length scale L and time by $T = L/U$, where U is a chosen velocity scale. We choose $L = 5000$ km and $U = 40\ \mathrm{m\,s^{-1}}$ for which the nondimensional time unit is $T = 1.5$ day and the nondimensional terrestrial midlatude value of β is 10. Turbulence is maintained by stochastic forcing. The structure of the imposed forcing is specified by the function F and its amplitude by the scalar f. This spatially and temporally homogeneous forcing will be specified later.

Velocity fields are decomposed into zonal-mean components (indicated upper case) and perturbations (indicated lowercase and primes) so that the zonal velocity is $U(y,t) + u'(x,y,t)$, the meridional velocity is $v'(x,y,t)$, and the vorticity is $Q(y,t) + q'(x,y,t)$. Averaging in the zonal direction is denoted with a bar. Taking the zonal average of Eq. (2.1) we obtain two coupled equations for the evolution of the mean flow, U, and the associated perturbation field:

$$\partial_t U = \overline{v'q'} - r_{\mathrm{m}} U \ , \tag{2.2a}$$

$$\partial_t q' = -U \partial_x q' + (U_{yy} - \beta)\, \partial_x \psi' - r q' - \nu_4 \Delta^2 q' + F_e + \sqrt{f} F \ , \tag{2.2b}$$

where

$$F_e = \left(\partial_y \left(\overline{v'q'} \right) - \partial_y (v'q') \right) - \partial_x (u'q') \tag{2.3}$$

is the nonlinear term representing the perturbation-perturbation interactions. In the above equation $\psi' = \Delta^{-1} q'$, where Δ^{-1} is the inverse of the Laplacian $\Delta \equiv \partial^2_{xx} + \partial^2_{yy}$. The mean flow and perturbation Eqs. (2.2) define the nonlinear system (which will be referred to as NL). In Eqs. (2.2) the damping rates r and r_{m} may differ. Hyperviscosity is included in the perturbation equations for numerical stability and forcing is applied only to the perturbation equations.

3. Formulation of quasi-linear barotropic dynamics on a beta-plane

The QL approximation of NL (2.2) is obtained by parameterizing the perturbation-perturbation nonlinearity in Eq. (2.2*b*) as a state independent stochastic excitation and retaining the nonlinear Reynolds stress forcing, $\overline{v'q'}$, in the mean zonal flow equation to obtain the quasi-linear (QL) system:

$$\partial_t U = \overline{v'q'} - r_{\mathrm{m}} U \ , \tag{3.1a}$$

$$\partial_t q' = -U \partial_x q' + (U_{yy} - \beta)\, \partial_x \psi' - r q' - \nu_4 \, \Delta^2 q' + \sqrt{f} F \ , \tag{3.1b}$$

where F gives the spatial and temporal structure of the stochastic excitation.

The perturbation-perturbation nonlinearity, F_e, redistributes energy and enstrophy among the eddy scales. It can be shown that both the complete system (2.2) and its QL approximation (3.1) conserve both energy and enstrophy in the absence of forcing and dissipation.

Because in Eqs. (3.1) U is not a function of x, and the perturbation-perturbation nonlinearity has been neglected, the perturbation vorticity, q', can be represented as a sum of non-interacting zonal harmonics

$$q'(x,y,t) = \mathrm{Re}\left[\sum_{k=1}^{N_k} \hat{q}_k(y,t) e^{\mathrm{i}kx}\right] \ , \tag{3.2}$$

where Re denotes the real part and $1,\ldots,N_k$ are the zonal wavenumbers excited by the stochastic forcing in (3.1*b*). The structure of the stochastic forcing is expanded as:

$$F(x,y,t) = \mathrm{Re}\left[\sum_{k=1}^{N_k} \hat{F}_k(y,t) e^{\mathrm{i}kx}\right] \ . \tag{3.3}$$

The stochastic forcing $\hat{F}_k(y,t) = \sum_{\ell=1}^{N_y} \mathrm{F}_{k\ell}(y)\, \xi_{k\ell}(t)$ excites each of the $\mathrm{F}_{k\ell}(y)$ (to be specified) with coefficient $\xi_{k\ell}(t)$. The $\xi_{k\ell}$ are temporally δ-correlated and independently excite both the zonal harmonics and the meridional structures and are prescribed by:

$$\left\langle \xi_{k\ell}(t) \right\rangle = 0 \quad , \quad \left\langle \xi_{k\ell}(t) \xi^*_{mn}(t') \right\rangle = \delta_{km} \delta_{\ell n}\, \delta(t-t') \ , \tag{3.4}$$

where the angle bracket denotes an ensemble average over realizations.

The two-point perturbation vorticity covariance is defined as:

$$C(x_a, y_a, x_b, y_b, t) = \left\langle q'(x_a, y_a, t) q'(x_b, y_b, t) \right\rangle \ . \tag{3.5}$$

Because of the independence of the excitations, $\xi_{k\ell}$, and the separability of the linear dynamics (3.1*b*) in x, the covariance is homogeneous in the zonal direction at all times and can be expanded in the difference coordinate, $x_a - x_b$, as:

$$\begin{aligned} C(x_a - x_b, y_a, y_b, t) &= \frac{1}{2}\, \mathrm{Re}\left[\sum_{k=1}^{N_k} \left\langle \hat{q}_k(y_a,t) \hat{q}^*_k(y_b,t) \right\rangle e^{\mathrm{i}k(x_a - x_b)}\right] \\ &= \frac{1}{2}\, \mathrm{Re}\left[\sum_{k=1}^{N_k} \hat{C}_k(y_a, y_b, t)\, e^{\mathrm{i}k(x_a - x_b)}\right] \ , \end{aligned} \tag{3.6}$$

where $\hat{C}_k(y_a, y_b, t)$ is the latitudinal covariance of the vorticity field at zonal wavenumber k and time t.

The spatial covariance of the forcing is defined as

$$Q(x_a, x_c, y_b, y_d) = \left\langle F(x_a, y_b, t) F(x_c, y_d, t) \right\rangle \ , \tag{3.7}$$

and is assumed to be homogeneous in both x and y, with the Fourier expansion:

$$Q(x_a - x_c, y_b - y_d) = \text{Re}\left[\sum_{k=1}^{N_k}\sum_{\ell=1}^{N_y} \hat{Q}_{k\ell}\, e^{\mathrm{i}\left[k(x_a - x_c) + \ell(y_b - y_d)\right]}\right] \ . \tag{3.8}$$

At zonal wavenumber k, the corresponding latitudinal spatial covariance is:

$$\hat{Q}_k(y_a, y_b) = \sum_{\ell=1}^{N_y} \hat{Q}_{k\ell}\, e^{\mathrm{i}\ell(y_b - y_d)} \ . \tag{3.9}$$

4. Formulation of SSST barotropic dynamics on a beta-plane

Taking the Fourier transform of Eq. (3.1*b*) and discretizing the fields on a meridional grid we obtain the corresponding matrix form:

$$\partial_t \hat{\boldsymbol{q}}_k = \mathsf{A}_k(\boldsymbol{U})\ \hat{\boldsymbol{q}}_k + \sqrt{f}\,\hat{\boldsymbol{F}}_k \ , \tag{4.1}$$

with

$$\mathsf{A}_k(\boldsymbol{U}) = -\mathrm{i}k\left[\mathsf{U} - (\mathsf{U}_{yy} - \beta\mathsf{I})\,\mathsf{\Delta}_k^{-1}\right] - r\mathsf{I} - \nu_4\mathsf{\Delta}_k^2 \ . \tag{4.2}$$

The state, $\hat{\boldsymbol{q}}_k$; the zonal mean flow, $\boldsymbol{U}$; and the Fourier coefficient of the forcing, $\hat{\boldsymbol{F}}_k$; are column vectors with elements the values at the N_y discretization points, y_j. In the matrix A_k, $\mathsf{\Delta}_k = \mathsf{D}^2 - k^2\mathsf{I}$, with D^2 the discretized ∂_{yy} operator, I the identity matrix, $\mathsf{\Delta}_k^{-1}$ the inverse of $\mathsf{\Delta}_k$, U the diagonal matrix with diagonal elements $\boldsymbol{U}$ and U_{yy} the diagonal matrix with diagonal elements $\mathsf{D}^2\boldsymbol{U}$. With this discretization the latitudinal covariance $\hat{C}_k(y_a, y_b, t)$ of Eq. (3.6) becomes the matrix $\mathsf{C}_k = \left\langle \hat{\boldsymbol{q}}_k \hat{\boldsymbol{q}}_k^\dagger \right\rangle$, with † denoting the Hermitian transpose.

The meridional spatial structure of the forcing, $\hat{\boldsymbol{F}}_k$, is specified by a matrix F_k, so that for each k, the white noise $\xi_{k\ell}$ excites the spatial structure given by the ℓ-th column of F_k. Consequently, the forcing of the k-th wavenumber is written as:

$$[\hat{\boldsymbol{F}}_k]_j = \sum_{\ell=1}^{N_y}\left[\mathsf{F}_k\right]_{j\ell}\xi_{k\ell}(t) \ . \tag{4.3}$$

The structure of the forcing is determined by F_k, and the forcing structures have been normalized, as will be described.

The dynamical equation for the ensemble average of the covariance of the perturbations in Eq. (4.1), C_k, satisfies the time dependent Lyapunov equation:

$$\partial_t \mathsf{C}_k = \mathsf{A}_k(\boldsymbol{U})\mathsf{C}_k + \mathsf{C}_k\mathsf{A}_k(\boldsymbol{U})^\dagger + f\mathsf{Q}_k \ , \tag{4.4}$$

as in Farrell & Ioannou (1996). The overall forcing amplitude is controlled by the parameter f and the spatial covariance of the forcing enters this equation as $\mathsf{Q}_k = \mathsf{F}_k\mathsf{F}_k^\dagger$, or equivalently in terms of the spectral coefficients of the forcing covariance, $\hat{Q}_{k\ell}$, as:

$$\left[\mathsf{Q}_k\right]_{bd} = \sum_{\ell=1}^{N_y}\hat{Q}_{k\ell}\, e^{\mathrm{i}\ell(y_b - y_d)} \ . \tag{4.5}$$

The covariances, C_k, determine the second order statistics of all perturbation fields. For example, the ensemble average of the vorticity flux,

$$\langle v'q'\rangle = \sum_{k=1}^{N_k}\frac{1}{2}\,\text{Re}\left(\left\langle \hat{v}_k\hat{q}_k^*\right\rangle\right) \ , \tag{4.6}$$

is expressed in terms of the covariances, C_k, as:

$$\begin{aligned} \boldsymbol{vq} &= -\sum_{k=1}^{N_k} \frac{k}{2}\,\mathrm{vecd}\left[\mathrm{Im}\left(\left\langle \mathsf{\Delta}_k^{-1}\hat{\boldsymbol{q}}_k\hat{\boldsymbol{q}}_k^{\dagger}\right\rangle\right)\right] \\ &= -\sum_{k=1}^{N_k} \frac{k}{2}\,\mathrm{vecd}\left[\mathrm{Im}\left(\mathsf{\Delta}_k^{-1}\mathsf{C}_k\right)\right]\ , \end{aligned} \tag{4.7}$$

where $\boldsymbol{vq}$ is the column vector of the values of $\langle v'q'\rangle$ and Im denotes the imaginary part. We denote with vecd (M) the column vector consisting of the diagonal elements of matrix M.

Under the ergodic assumption that the zonal average of the perturbation covariance can be obtained from the ensemble average, we substitute $\overline{v'q'} = \langle v'q'\rangle$ in Eq. (3.1a) to obtain an equation for the evolution of the zonal mean, which is linear in the C_k:

$$\partial_t \boldsymbol{U} = -\sum_{k=1}^{N_k} \frac{k}{2}\,\mathrm{vecd}\left[\mathrm{Im}\left(\mathsf{\Delta}_k^{-1}\mathsf{C}_k\right)\right] - r_{\mathrm{m}}\boldsymbol{U}\ . \tag{4.8}$$

The system of equations formed by (4.4) and (4.8), define the SSST dynamics for the evolution of the zonally averaged flow, $\boldsymbol{U}$, and its associated ensemble average perturbation covariances, C_k:

$$\partial_t \boldsymbol{U} = -\sum_{k=1}^{N_k} \frac{k}{2}\,\mathrm{vecd}\left[\mathrm{Im}\left(\mathsf{\Delta}_k^{-1}\mathsf{C}_k\right)\right] - r_{\mathrm{m}}\boldsymbol{U}\ , \tag{4.9a}$$

$$\partial_t \mathsf{C}_k = \mathsf{A}_k(\boldsymbol{U})\,\mathsf{C}_k + \mathsf{C}_k\,\mathsf{A}_k(\boldsymbol{U})^{\dagger} + f\,\mathsf{Q}_k\ . \tag{4.9b}$$

5. Specification of the stochastic forcing

Three stochastic forcing structures will be used in our investigation of the correspondence of SSST, QL and NL dynamics.

The first independently excites a set of zonal wavenumbers. This forcing was first used by Williams (1978) to parameterize excitation of barotropic dynamics by baroclinic instabilities. This method of forcing was also used by DelSole (2001) in his study of upper-level tropospheric jet dynamics and in the study of jet formation using SSST dynamics by Farrell & Ioannou (2003, 2007) and Bakas & Ioannou (2011). This stochastic forcing is spatially homogeneous but not isotropic.

The second is an isotropic ring forcing concentrated near a single total wavenumber. This forcing structure has been used extensively in studies of beta-plane turbulence (cf. Vallis & Maltrud 1993) and was also been used in the recent study of Srinivasan & Young (2012). It was introduced by Lilly (1969), in order to isolate the inverse cascade from the forcing in a study of two dimensional turbulence.

The third is an isotropic ring forcing, similar to the second, but with the forcing distributed over a wider annular region around the central wavenumber.

Recall that the stochastic forcing,

$$F(x_i, y_j, t) = \mathrm{Re}\left[\sum_{k=1}^{N_k}\sum_{\ell=1}^{N_y}\left[\mathsf{F}_k\right]_{j\ell}\,\xi_{k\ell}(t)\,e^{\mathrm{i}kx_i}\right]\ , \tag{5.1}$$

is correlated in y by the columns of the matrix F_k. For the non-isotropic forcing (NIF) this meridional structure of the forcing correlation, in a channel periodic and of length 2π in y, is specified by:

$$\left[\mathsf{F}_k\right]_{j\ell} = c_k \left[e^{-(y_j-y_\ell)^2/(2s^2)} + e^{-(y_j-2\pi-y_\ell)^2/(2s^2)} + e^{-(y_j+2\pi-y_\ell)^2/(2s^2)} \right] . \tag{5.2}$$

Each forcing is Gaussian correlated in y, with half-width $s = 0.2/\sqrt{2}$ and we force zonal waves $k = 1, \ldots, 14$. Because the stochastic forcing is δ-correlated in time, the energy injection rate does not depend on the state and can be independently specified (cf. Appendix B). The normalization constant, c_k, in (5.2) is chosen so that each k is excited equally and one unit of energy is injected in total, so that f is the total energy injection rate in the NL, QL or SSST simulations.

The isotropic ring forcing is specified by:

$$\left[\mathsf{F}_k\right]_{j\ell} = c\, w_{k\ell}(K)\, e^{\mathrm{i}\ell y_j} , \tag{5.3}$$

with $K = \sqrt{k^2+\ell^2}$. Because the channel is square with length 2π, both k and ℓ are integers and only integer wavenumbers are excited. The first isotropic forcing (IRFh) is specified by

$$w_{k\ell} = \left\{ \begin{array}{ccc} 1 & , & |K-K_f| \leqslant \delta k_f \ , \\ 0 & , & |K-K_f| > \delta k_f \ . \end{array} \right. \tag{5.4}$$

For IRFh we choose $K_f = 14$ and $\delta k_f = 1$. The second forcing (IRFg) is specified as:

$$w_{k\ell} = c\, \exp\left[-\frac{(K-K_f)^2}{2\,\delta k_f^2} \right] . \tag{5.5}$$

For IRFg we choose $K_f = 14$ and $\delta k_f = 8$. The normalization constant, c, is chosen so that the total energy injection rate is unity (cf. Appendix B). IRFh and IRFg are both spatially homogeneous and nearly isotropic in a finite doubly periodic domain. They approach exact isotropy as the domain size increases.

Plots of the corresponding power spectra together with instantaneous realizations of the stochastic forcing both in vorticity and streamfunction are shown in figure 1 for the three types of forcing structures. The thin IRFh ring forcing primarily excites vortices of scale $1/K_f$ in the flow that are evident in both the vorticity and streamfunction fields, while IRFg produces a streamfunction field dominated by large scale structure.

6. Stability of the SSST homogeneous equilibrium state

Because of the homogeneity of the stochastic forcing, $\boldsymbol{vq} = 0$ in the absence of symmetry breaking by a mean flow, and the SSST equations admit the homogeneous equilibrium solution:

$$\boldsymbol{U}^E = 0 \quad , \quad \mathsf{C}^E = \sum_{k=1}^{N_k} \mathsf{C}_k^E \quad \text{with} \quad \mathsf{C}_k^E = \frac{f}{2r} \mathsf{Q}_k \ , \tag{6.1}$$

for $\nu_4 = 0$. The stability of this equilibrium state, $(\boldsymbol{U}^E, \mathsf{C}^E)$, is determined by the linear dynamics of the evolution of perturbations $(\delta\boldsymbol{U}, \delta\mathsf{C}_1, \ldots, \delta\mathsf{C}_{N_k})$ to this equilibrium. These perturbations satisfy the linear equations:

$$\partial_t\,\delta\boldsymbol{U} = -\sum_{k=1}^{N_k}\frac{k}{2}\,\mathrm{vecd}\left[\,\mathrm{Im}\,(\mathsfit{\Delta}_k^{-1}\delta\mathsfit{C}_k)\right] - r_{\mathrm{m}}\delta\boldsymbol{U}\ , \tag{6.2a}$$

$$\partial_t\,\delta\mathsfit{C}_k = \mathsfit{A}_k^E\delta\mathsfit{C}_k + \delta\mathsfit{C}_k\left(\mathsfit{A}_k^E\right)^\dagger + \delta\mathsfit{A}_k\mathsfit{C}_k^E + \mathsfit{C}_k^E\left(\delta\mathsfit{A}_k\right)^\dagger\ , \tag{6.2b}$$

which are obtained by linearizing the SSST system (4.9) about $(\boldsymbol{U}^E, \mathsfit{C}^E)$. In the above equations $\mathsfit{A}_k^E \equiv \mathsfit{A}_k(\boldsymbol{U}^E)$ is the operator linearized about the equilibrium mean zonal flow, $\boldsymbol{U}^E$, and $\delta\mathsfit{A}_k$ is $\delta\mathsfit{A}_k = -\mathrm{i}k\left[\delta\mathsfit{U} - (\delta\mathsfit{U})_{yy}\,\mathsfit{\Delta}_k^{-1}\right]$. Eigenfunctions of the form,

$$(\delta\boldsymbol{U}, \delta\mathsfit{C}_1, \ldots, \delta\mathsfit{C}_{N_k})\,e^{\sigma t}\ , \tag{6.3}$$

satisfy the following eigenvalue problem:

$$\sigma\,\delta\boldsymbol{U} = -\sum_{k=1}^{N_k}\frac{k}{2}\,\mathrm{vecd}\left[\,\mathrm{Im}\,(\mathsfit{\Delta}_k^{-1}\delta\mathsfit{C}_k)\right] - r_{\mathrm{m}}\delta\boldsymbol{U}\ , \tag{6.4a}$$

$$\sigma\,\delta\mathsfit{C}_k = \mathsfit{A}_k^E\delta\mathsfit{C}_k + \delta\mathsfit{C}_k\left(\mathsfit{A}_k^E\right)^\dagger + \delta\mathsfit{A}_k\mathsfit{C}_k^E + \mathsfit{C}_k^E\left(\delta\mathsfit{A}_k\right)^\dagger\ . \tag{6.4b}$$

The equilibrium $(\boldsymbol{U}^E, \mathsfit{C}^E)$ is stable when all the eigenvalues of system (6.4) satisfy $\sigma_r = \mathrm{Re}\,(\sigma) \leqslant 0$. Otherwise, the SSST equilibrium is unstable and the SSST system bifurcates to a structurally distinct attractor.

The eigenfunctions and eigenvalues of Eqs. (6.4) are readily obtained in the case of the homogeneous equilibrium state (6.1). Because of the homogeneity of this equilibrium, the mean flow part of the eigenfunctions are sinusoidal with form $\delta U_n = \sin\,(ny)$. This perturbation of the mean flow consists of n pairs of alternating prograde and retrograde jets. For the case $\beta = 0$ the eigenvalues can be obtained analytically (Bakas & Ioannou 2011), otherwise both the eigenfunction, $\delta\mathsfit{C}_{k,n}$, and the eigenvalue, $\sigma(n)$, can be obtained iteratively by introducing $\delta U_n = \sin\,(ny)$, which specifies $\delta\mathsfit{A}_{k,n}$ in (6.4b), obtaining $\delta\mathsfit{C}_{k,n}$ from the resulting Sylvester equation:

$$\left[\mathsfit{A}_k^E - \sigma(n)\mathsfit{I}\right]\delta\mathsfit{C}_{k,n} + \delta\mathsfit{C}_{k,n}\left(\mathsfit{A}_k^E\right)^\dagger = -\left[\delta\mathsfit{A}_{k,n}\mathsfit{C}_k^E + \mathsfit{C}_k^E\left(\delta\mathsfit{A}_{k,n}\right)^\dagger\right]\ , \tag{6.5}$$

introducing $\delta\mathsfit{C}_{k,n}$ in Eq. (6.4a) and continuing this iteration until convergence is obtained.

We now investigate the stability of the homogeneous equilibrium state (6.1) as a function of the forcing amplitude, f. In the absence of forcing, $f = 0$, Eqs. (6.4) decouple and all mean flow perturbations decay with $\sigma(n) = -r_{\mathrm{m}}$. In the presence of forcing the mean zonal flow perturbations are coupled to the perturbation covariance and this coupling may give rise to an SSST instability. We will demonstrate that such a structural instability occurs for forcing amplitudes $f > f_c$ resulting to transition to an inhomogeneous equilibrium with finite amplitude zonal jets.

Growth rates, σ_r, are shown in figure 2 for NIF as a function of the meridional wavenumber of the mean zonal flow perturbation, n, and of the forcing amplitude, f, and similarly for IRFh in figure 3. For both types of forcing, instability occurs for $f > f_c$ over a band of mean flow wavenumbers, n. In all cases the $\sigma(n)$ associated with the largest growth rate has zero imaginary part. Growth rate curves are shown in figure 4 for various forcings and damping amplitudes. In the next section the predictions of this SSST stability analysis will be compared with the corresponding QL and NL simulations. While QL and NL simulations can not provide theoretical predictions for the bifurcation structure of turbulent equilibria, we wish to examine the circumstances under which the underlying bifurcation structure revealed by SSST is reflected in the QL and NL realizations.

7. Bifurcations predicted by SSST and their reflection in QL and NL simulations

We examine the reflection of the SSST structural instability in NL and QL simulations by comparing the evolution of the domain averaged energy of the zonal flow:

$$E_m(t) = \frac{1}{L_x L_y} \iint \frac{1}{2} U^2 \, \mathrm{d}x \, \mathrm{d}y \ . \tag{7.1}$$

The amplitude of the zonal flow is measured with the zonal mean flow index (zmf) defined as $\text{zmf} = E_m/(E_m + E_p)$, where E_m is the time averaged energy of the zonal mean flow, given in Eq. (7.1), and E_p is the time average of the domain average kinetic energy of the perturbations

$$E_p(t) = \frac{1}{L_x L_y} \iint \frac{1}{2} \left(u'^2 + v'^2 \right) \, \mathrm{d}x \, \mathrm{d}y \ . \tag{7.2}$$

7.1. *Correspondece of jet emergence in NL, QL and SSST for moderate damping*

The case of NIF with $r = 0.1$, $r_\mathrm{m} = 0.01$ and $f = 1.5 f_c$ is plotted in figure 5. For this forcing and parameters, SSST predicts that maximum growth occurs for the sinusoidal zonal mean flow perturbation with $n = 6$, as seen in figure 4a. Introduction of this eigenfunction in the SSST dynamics produces initially the predicted exponential growth, followed by approach to an equilibrium consisting of 6 finite amplitude jets. This equilibration demonstrates that the SSST dynamics includes the mechanism of stabilization of the SSST instability. Corresponding simulations with the QL and NL dynamics using the same parameters for the damping and the forcing reveal nearly identical jet growth followed by finite amplitude equilibration. A Hovmöller diagram showing the development of the mean flow associated with the SSST instability is shown in figure 6, together with corresponding diagrams for the development of the associated mean flow in the QL and NL simulations. Although no theoretical prediction of this bifurcation behavior can be made directly from the QL or the NL dynamics, they both reveal the bifurcation structure obtained from the SSST analysis.

At larger forcing amplitudes the SSST jet formation instability typically equilibrates at a wavenumber smaller than that of the instability. An example for NIF at supercriticality $f = 20 f_c$ is shown in figure 7. While the jets emerge initially with zonal wavenumber $n = 6$ (cf. figure 4b), in agreement with the prediction of SSST instability, the zonal flow eventually equilibrates at wavenumber $n = 4$, following a series of mergers that are evident in the Hovmöller diagrams. This behavior can be rationalized by noting that as the jet amplitude increases at a fixed wavenumber, violation of the Rayleigh-Kuo stability criterion occurs, at which point, by transitioning to a lower wavenumber, the flow forestalls occurrence of an inflectional instability (Farrell & Ioannou 2007). However, SSST stability analysis of the finite amplitude equilibria near the point of jet merger reveals that these mergers coincide with the inception of a structural instability, which precedes the occurrence of hydrodynamic instability of the jet (Farrell & Ioannou 2003).

A plot of the zonal mean flow indices (zmf) in the NL and QL simulations and in the associated SSST equilibria are shown in figure 8 as a function of forcing amplitude for NIF forcing of $k = 1, \dots, 14$ with damping parameters $r = 0.1$, $r_\mathrm{m} = 0.01$. Consistent with the specific examples shown in figure 6 and figure 7, this figure demonstrates that the SSST bifurcation structure is paralleled by the QL and NL simulations over a wide range of forcing amplitudes. It also demonstrates that both the NL and QL simulations equilibrate at finite amplitude with nearly the same structure as the SSST equilibria.

Similar agreement is obtained with IRFh at $K_f = 14$ with $\delta k_f = 1$ and damping parameters $r = 0.1$, $r_{\mathrm{m}} = 0.01$ for which the case with $f = 2.5f_c$ is shown in figure 9. Maximum growth occurs at zonal wavenumber $n = 8$ in this case (cf. figure 4c) and again the SSST predictions for both initiation of the instability and its saturation are reflected in the QL and NL simulations. The bifurcation diagram for this IRFh forcing and damping is plotted in figure 10. For this case also the critical amplitude, f_c, is correctly predicted by SSST stability analysis, but for supercritical forcing amplitudes the zonal flow predicted by SSST and QL is stronger and the perturbation energy smaller than the corresponding zonal flow and perturbation energy obtained in the NL simulations. This difference between the NL and both the SSST predictions and QL simulations at high levels of forcing, corresponding to high superctiticality, is in part accounted for by the spreading of the spectrum in NL as shown in figure 10, where the zmf index that results when the SSST is forced by the NL spectrum at $f = 20f_c$ is shown. However, the major part of this difference is due to the nonlinear perturbation-perturbation interactions in NL that disrupt the upgradient momentum transfer. This disruption is accentuated by the peculiar efficiency with which the narrow ring forcing, IRFh, gives rise to vortices as can seen in figure 1 (middle panel). We verify that this narrow ring forcing is responsible for depressing NL equilibrium jet strength at high superctiticality by broadening the forcing distribution in the form of IRFg for which $K_f = 14$ and $\delta k_f = 8$. Using this modified forcing we obtain agreement between SSST, QL and NL simulations with the same parameters as those used in figure 10, as is shown in figure 11.

7.2. *Correspondence of jet emergence in NL, QL and SSST for weak damping*

For sufficiently small perturbation damping, r, the SSST critical forcing amplitude, f_c, for jet emergence differs from the critical forcing amplitude, $f_c^{(\mathrm{NL})}$, at which finite amplitude and persistent zonal mean flows form in the NL simulations. For example, for perturbation damping $r = 0.01$ the NL simulations bifurcate at $f_c^{(\mathrm{NL})} \approx 11f_c$ under NIF forcing with $k = 1, \ldots, 14$ and at $f_c^{(\mathrm{NL})} \approx 4f_c$ under IRFh forcing at $K_f = 14$ and $\delta k_f = 1$. Similar behavior was noted by Srinivasan & Young (2012). The bifurcation diagram for the NIF forcing is shown in figure 12 and for the IRFh forcing in figure 13. The reason for the difference in the NL and SSST bifurcation curves will be explained in section 8. Typical structure of the emerging jets for the IRFh forcing is shown in figure 14.

8. Development of the turbulence spectra in nonlinear simulations and their influence on SSST stability

Both QL and SSST dynamics exclude interactions among perturbations and include only the non-local interactions between zonally averaged quantities, with $k = 0$, and perturbations, with $k \neq 0$. Therefore, there is no enstrophy or energy cascade in wavenumber space in QL and SSST dynamics and the equilibrium state in SSST, ($U^E = 0$ and $C^E = f \sum_{k=1}^{N_k} Q_k/2r$), has a spectrum proportional to the spectrum of the forcing, which is fully prescribed by the forcing covariances, Q_k. However, this is not true in NL dynamics which includes perturbation-perturbation interactions producing enstrophy/energy cascades. For example, in NL an isotropic ring forcing is distorted as time progresses by the nonlinear perturbation-perturbation interactions becoming concentrated at lower wavenumbers and forming the characteristic dumbbell shape seen in beta-plane turbulence simulations (Vallis & Maltrud 1993), as shown in figure 15. It is to be expected that the statistical equilibrium state obtained by NL dynamics will be different from the corresponding SSST equilibrium state due to this difference in the spectrum. The equilibrium spectrum obtained by taking a time average of long NL simulations, in which the

$k = 0$ component of the flow has been set to zero, is shown in figure 16 for various forcing amplitudes and damping rates. The departure of the NL spectra from the spectra of the QL and SSST equilibria is evident and this difference depends on the amplitude of the forcing and the linear damping coefficient, r. A necessary condition for obtaining agreement between NL and both SSST and QL dynamics is that the equilibrium spectrum of the SSST and QL dynamics be close to the equilibrium spectrum in the NL dynamics so that the stability analysis is performed on similar states.

The equilibrium spectrum obtained in the NL simulation does not differ appreciably from the spectrum of the forcing for IRFh at $K_f = 14$ with $\delta k_f = 1$ and linear damping $r = 0.1$ (cf. figure 16). In such cases SSST successfully predicts the critical parameters for the emergence of jet structure in NL simulations as shown by the bifurcation diagram in figure 10 and, for the case of NIF, in figure 8.

SSST dynamics can be shown to accurately predict the emergence of zonal mean flows in the more weakly dissipated regime with $r = 0.01$, for which the NL spectra depart significantly from the spectra of the SSST homogeneous equilibrium, by performing the SSST stability analysis on the equilibrium spectrum obtained in the NL dynamics prior to emergence of the zonal mean jets. For example, with IRFh at $K_f = 14$ and $\delta k_f = 1$ and perturbation dissipation $r = 0.01$, formation of persistent finite amplitude zonal mean flows occurs in the NL simulations in the range $3f_c < f < 4f_c$ instead of at f_c (cf. figure 13). We perform an SSST stability analysis with forcing covariance associated with the spectrum $f\hat{Q}_{k\ell} = 2r\langle|\hat{q}_{k\ell}|^2\rangle$, where $\langle|\hat{q}_{k\ell}|^2\rangle$ is the enstrophy spectrum obtained from the NL simulations in which the $k = 0$ component was removed. We find that the equilibrium state with this spectrum is more stable than the original isotropic ring SSST equilibrium. This can be seen in figure 17 in which the growth rate of the SSST instability is shown as a function of the meridional wavenumber of the zonal mean perturbations for various forcing amplitudes. This calculation reveals that the NL-equivalent SSST equilibrium is marginally stable for $f = 2.8f_c$, and the NL modified spectrum produces SSST instability for $f \geqslant 2.8f_c$. This result agrees with the NL simulations which show the emergence of persistent zonal mean flows for $f \geqslant 2.8f_c$. Moreover, SSST stability analysis on this NL-equivalent equilibrium state predicts that the zonal mean flow instability will occur at meridional wavenumber $n = 5$ or $n = 6$, while the maximal instability for the isotropic ring spectrum that characterizes the corresponding SSST equilibrium occurs at the higher wavenumber $n = 8$ (cf. figure 4d). In agreement with these predictions, zonal mean flows emerge in the NL simulations at $f = 10f_c$ with $n = 6$ while in both the QL and SSST simulation zonal mean flows emerge with $n = 9$, and equilibrate to a finite amplitude zonal mean flow with $n = 6$, as shown in figure 14. We find in addition that the reduced amplitude of the zonal flows seen in the NL simulations (cf. figures 12 and 13) can also be traced to the modification of the forcing spectrum by the nonlinear processes which reduces the forcing from the eddy field. The zmf that results in SSST using the NL modified spectrum is shown in figures 12 and 13 to agree with zmf obtained in the NL simulations†. This demonstrates that differences between the predictions of SSST stability theory and NL simulations for the emergence of zonal mean flows under weak damping results from the distortion of the equilibrium spectrum by the nonlinear interactions in the NL simulations.

---

† The NL modified spectrum used to obtain the SSSTb bifurcation curve shown in figure 12 was obtained from the NL equilibrium spectrum at $f = 4f_c$. The spectrum used in figure 13 was obtained by similar means using an NL simulation at $f = 2f_c$ (both with the k=0 component removed). The results are not sensitive to the choice of spectrum as long the broadening of the spectrum has been represented.

We can appreciate the control that the perturbation spectrum exerts on jet emergence by examining the case of forcing amplitude $f = 2f_c$ with IRFh. For this forcing amplitude, the SSST is structurally unstable and both SSST and QL simulations equilibrate to finite amplitude jets, as shown in figure 18. SSST stability analysis performed on the NL modified spectra (cf. figure 19) shows that for this forcing amplitude, the asymptotic spectrum is subcritical to structural instability (cf. the SSST growth rates on the approximately asymptotic $t = 250$ spectrum in figure 20). Consistent with this asymptotic stability, the NL simulation does not support coherent persistent jets (cf. figure 18). However, while in the NL simulation no coherent jets are seen, clear indications of jet structure can be seen, although these jets are intermittent in both space and time. In order to understand these observations we perform SSST stability analysis on the spectrum as it develops in the NL simulation. The developing spectrum, shown in figure 19, is obtained from a simulation initialized with a perturbation and mean flow free state and the corresponding SSST growth rates associated with the developing spectrum are shown in figure 20. By $t = 20$ the NL spectrum, having assumed the isotropic ring structure of the forcing, becomes SSST unstable. This structural instability is evident in the incipient formation of jet structure in the NL simulation at $t = 50$ in figure 18. As the spectrum further evolves, the SSST growth rates fall and the spectrum supports only stable modes for $t > 120$, with decay rates asymptotically approaching those corresponding to $t = 250$ in figure 20. For these asymptotic perturbation spectra, SSST stability analysis reveals a manifold of decaying modes among which the least damped modes are jets with meridional wavenumber $n = 5, 6, 7, 8$. There is clear evidence of zonal structure in the NL simulations in the form of a superposition of the $n = 5, 6, 7, 8$ least damped modes of the SSST stability analysis (cf. figure 17). These damped modes are excited by the fluctuations associated with realizations of the stochastic forcing in NL simulations. Similar excitation of intermittent jets associated with these damped modes arise in QL simulations with SSST subcritical stochastic forcing. An example simulation (cf. figure 21) shows these intermittent jets both in QL and NL simulations under SSST subcritical forcing. Confirmation that these intermittent jets result from fluctuation excitation of the SSST damped modes is given in the bottom panel of figure 21, where the intermittent jets resulting from stochastic forcing of the SSST modes themselves are shown. This diagram was obtained by plotting

$$U(y,t) = \mathrm{Re}\left[\sum_{n=1}^{N} \alpha_n(t) e^{\mathrm{i}ny}\right] , \tag{8.1}$$

with α_n independent red noise processes, associated with the damping rates, $-\sigma(n)$, of the first $N = 15$ SSST least damped modes. These α_n are obtained from the Langevin equation,

$$\frac{\mathrm{d}\alpha_n}{\mathrm{d}t} = \sigma(n)\,\alpha_n + \xi(t) \ , \tag{8.2}$$

with $\xi(t)$ a δ-correlated complex valued random variable.

The fluctuation-free SSST simulations reveal persistent jet structure by the inception of the SSST instability only at supercritical forcing. However, in the QL and NL simulations fluctuations excite the damped manifold of modes predicted by the SSST analysis to exist at subcritical forcing amplitudes. This observation confirms the reality of the wave/mean flow interaction manifold of stable modes. Moreover, the emergence of structure in subcritical simulations may be related to the observation of the so-called latent zonal jets in the oceans (Berloff *et al.* 2009, 2011).

In NL and QL simulations these stable modes predicted by SSST are increasingly excited as the critical bifurcation point in parameter space is approached, because their damping rate vanishes at the bifurcation. The associated increase in mean flow energy on approach to the bifurcation in NL and QL simulations, obscures the exact location of the bifurcation point in NL and QL simulations compared to the fluctuation-free SSST simulations for which the bifurcation is exactly coincident with the inception of instability (i.e. figures 8, 10 and 11).

SSST dynamics not only predicts the emergence of zonal jets but also predicts the finite amplitude equilibrium jets that result after the initial jet formation instability. These finite amplitude jets correspond to fixed points of the SSST dynamics. Here we compare the SSST predictions of finite amplitude jet structure with the results of NL and QL simulations. For the case of NIF (cf. figure 7), as well as for for IRFh and IRFg, the jet equilibria of the SSST dynamics are similar to the jets obtained in QL and NL simulations. An example for IRFh strongly forced with $f = 100 f_c$ and with damping $r = 0.01$ is shown in figure 22. This case demonstrates that a 20% difference in the zmf index alone between the NL, QL and SSST (cf. figure 13) is not reflected in a substantial disparity between jets in NL, QL and SSST simulations.

As is commonly found in nonlinear systems, the finite amplitude equilibria predicted by SSST are not necessarily uniquely determined and multiple equilibria can occur with the same parameters. SSST provides a method to explore these multiple equilibria and to determine their attractor basins in the parameter space. For supercritical parameter values the multitude of SSST instabilities with different zonal flow wavenumber (cf. Fig. 4) that occur may give rise to a multitude of finite equilibria jets. An example of two such SSST equilibria are shown in Fig. ..... with the corresponding NL simulations.

mergers as SSST instabilities

2003

are shown

each corresponding to a separate attractor basin. As the forcing superctiticality increases these equilibria SSST modes of instability that SSST also predicts the attractor basins of NL simulations. For small

9. Conclusions

In this work we compared the predictions of SSST for jet formation in barotropic beta-plane turbulence with QL and NL simulations. We found that the bifurcation structure predicted by SSST for the emergence of zonal jets from a homogeneous turbulent state is confirmed by both QL and NL simulations. Moreover, we showed that the finite amplitude equilibrium jets found in NL and QL simulations are as predicted by the fixed point solutions of SSST. Obtaining this agreement between NL and both SSST and QL simulations required that the modification of the turbulent spectrum caused by the perturbation-perturbation nonlinearity in NL be accounted for in the specification of the stochastic forcing in QL and SSST. These results confirm that jet emergence in barotropic beta-plane turbulence can be traced to the cooperative mean flow/perturbation instability that is captured by SSST. Moreover, the physical reality of the manifold of modes arising from cooperative interaction between incoherent turbulence and coherent jets, which is revealed by SSST, was verified in this work by relating the excitation of the spectrum of damped SSST modes to observations of latent jets in both QL and NL simulations. SSST provides an autonomous, deterministic nonlinear closure of the turbulent dynamics at second order that provides a vehicle for further analytic investigation of the dynamics of coherent structures in turbulent flows.

The authors would like to acknowledge discussions with N. Bakas, F. Bouchet, K. Srinivasan and W. Young. Navid Constantinou acknowledges the support of the Alexander S. Onassis Public Benefit Foundation. Brian Farrell was supported by NSF ATM-0123389. Brian Farrell and Petros Ioannou acknowledge the hospitality during June 2012 of the Aspen Center for Physics (supported by NSF under grant No. 1066293) where part of this paper was written. Petros Ioannou acknowledges the generous support of the John S. Latsis Foundation under "Research Projects 2011" .

Appendix A. Numerical details and parameters

Periodicity in the square channel $[0, 2\pi] \times [0, 2\pi]$ implies that the permissible zonal and meridional wavenumbers, (k, ℓ), are integers and the NIF and IRFh or IRFg forcing is limited to excite only these integer wavenumbers. The coefficient of linear damping for the mean flow in all simulations is $r_\mathrm{m} = 0.01$. The perturbations are either damped at the rate $r = 0.1$ or at the rate $r = 0.01$. In all simulations $\beta = 10$.

Both the nonlinear simulation (NL) Eq. (2.1) and the quasi-linear simulations (QL) of Eqs. (3.1) are done with a pseudospectral Fourier code. The maximum resolved wavenumbers are $k_\mathrm{max} = N_x/2$ and $\ell_\mathrm{max} = N_y/2$. For the time integration we use a fourth order Runge-Kutta method (RK4) using a Godunov step for integrating the stochastic forcing.

The coefficient of ν_4 is chosen for numerical stability as

$$\nu_4 = \frac{0.5}{K_\mathrm{max}^4\, \delta t} \ , \tag{A 1}$$

where $K_\mathrm{max}^4 = \Big[(N_x/2)^2 + (N_y/2)^2\Big]^2$ is the maximum resolved total wavenumber in the fourth power and δt is the time step. In all our calculations $\delta t = 2.5 \times 10^{-3}$, which implies $\nu_4 = 1.86 \times 10^{-7}$.

The stochastic forcing at the j-th time step is obtained from:

$$\xi_{km}(t_j) = \frac{\eta_j + \mathrm{i}\,\theta_j}{\sqrt{2\,\delta t}} \ , \tag{A 2}$$

where η_j and θ_j, $j = 1, 2, \dots$ are independent normally distributed random variables with zero mean and unit standard deviation. The phase of ξ_{km} is uniformly distributed on $[0, 2\pi]$. The $\sqrt{\delta t}$ in the denominator ensures that the forcing maintains constant variance as temporal resolution changes and the $\sqrt{2}$ ensures that ξ_{km} has unit variance, i.e. both ensure that in the limit $\delta t \to 0$ we obtain: $\int_{-\infty}^{\infty} \langle \xi_{km}(t) \xi_{km}^*(t') \rangle \, \mathrm{d}t' = 1$.

Appendix B. Calculation of the energy injection rate

The domain averaged energy injection rate by the stochastic forcing, F, is:

$$\varepsilon = -\sqrt{f} \int \frac{\mathrm{d}x}{L_x} \frac{\mathrm{d}y}{L_y}\, \psi' F \ . \tag{B 1}$$

We Fourier expand all fields as in (3.2). When y is discretized, the Fourier coefficient of the streamfunction, $\hat{\psi}_k(y,t)$, of the k zonal wavenumber, is related to vorticity coefficient, $\hat{q}_k(y,t)$, by $\hat{\boldsymbol{\psi}}_k(t) = \boldsymbol{\mathit{\Delta}}_k^{-1} \hat{\boldsymbol{q}}_k(t)$ where $\hat{\boldsymbol{\psi}}_k$ and $\hat{\boldsymbol{q}}_k$ are column vectors and $\boldsymbol{\mathit{\Delta}}_k^{-1}$ the inverse of the matrix representation of $\partial_{yy} - k^2$. The solution of Eq. (4.1) in matrix form is:

$$\hat{\boldsymbol{q}}_k(t) = \exp\big(\mathsf{A}_k t\big)\, \hat{\boldsymbol{q}}_k(0) + \sqrt{f} \int_0^t \exp\Big[\mathsf{A}_k (t-s)\Big] \mathsf{F}_k\, \boldsymbol{\xi}_k(s)\, \mathrm{d}s \ , \tag{B 2}$$

where $\boldsymbol{\xi}_k$ is the column vector with elements $\left[\boldsymbol{\xi}_k\right]_\ell = \xi_{k\ell}$. Assuming ergodicity, the zonal average in Eq. (B 1) can be replaced by an ensemble average and then converted in matrix form, obtaining:

$$\begin{aligned}
\varepsilon &= -\sqrt{f}\int\frac{\mathrm{d}y}{L_y}\left\langle\psi' F\right\rangle\\
&= -\sqrt{f}\int\frac{\mathrm{d}y}{L_y}\frac{1}{4}\left\langle\sum_{k=1}^{N_k}\left(\hat{\psi}_k\hat{F}_k^* + \hat{\psi}_k^*\hat{F}_k\right)\right\rangle\\
&= -\frac{\sqrt{f}}{N_y}\frac{1}{4}\left\langle\sum_{k=1}^{N_k}\mathrm{Tr}\left[\hat{\boldsymbol{\psi}}_k\left(\mathsf{F}_k\boldsymbol{\xi}_k\right)^\dagger + \left(\mathsf{F}_k\boldsymbol{\xi}_k\right)\hat{\boldsymbol{\psi}}_k^\dagger\right]\right\rangle\ ,
\end{aligned}\tag{B 3}$$

with Tr denoting the trace of a matrix. Because the noise processes are independent and temporally delta correlated, satisfying $\langle\xi_{km}(t)\xi^*_{k'm'}(t')\rangle = \delta_{kk'}\delta_{mm'}\delta(t-t')$, we obtain, using (B 2), that both terms of the sum in (B 3) are independent of the state of the system and equal to $-\frac{1}{2}\sqrt{f}\ \mathrm{Tr}\left(\varDelta_k^{-1}\mathsf{F}_k\mathsf{F}_k^\dagger\right)$. Consequently, energy is injected at the rate:

$$\varepsilon = \sum_{k=1}^{N_k}\varepsilon_k = \sum_{k=1}^{N_k} -\frac{f}{4N_y}\,\mathrm{Tr}\left(\varDelta_k^{-1}\mathsf{Q}_k\right)\ , \tag{B 4}$$

in the NL, QL and SSST simulations.

REFERENCES

Bakas, N. A. & Ioannou, P. J. 2011 Structural stability theory of two-dimensional fluid flow under stochastic forcing. *J. Fluid Mech.* **682**, 332–361.

Bakas, N. A. & Ioannou, P. J. 2012 On the mechanism underlying the spontaneous emergence of barotropic zonal jets. (submitted to J. Atmos. Sci.).

Baldwin, M. P., Rhines, P. B., Huang, H-P. & McIntyre, M. E 2007 The jet-stream conundrum. *Science* **39**, 467–468.

Berloff, P., Kamenkovich, I. & Pedlosky, J. 2009 A model of multiple zonal jets in the oceans: Dynamical and kinematical analysis. *J. Phys. Oceanogr.* **39**, 2711–2734.

Berloff, P., Karabasov, S., Farrar, J.T. & Kamenkovich, I. 2011 On latency of multiple zonal jets in the oceans. *J. Fluid Mech.* **686**, 534–567.

Bouchet, F. & Venaille, A. 2012 Statistical mechanics of two-dimensional and geophysical flows. *Physics Reports* **515** (5), 227 – 295.

Charney, J. G. & DeVore, J. G. 1979 Multiple flow equilibria in the atmosphere and blocking. *J. Atmos. Sci.* **36**, 1205–1216.

Connaughton, Colm P., Nadiga, Balasubramanya T., Nazarenko, Sergey V. & Quinn, Brenda E. 2010 Modulational instability of Rossby and drift waves and generation of zonal jets. *J. Fluid Mech.* **645**, 207–231.

DelSole, T. 2001 A simple model for transient eddy momentum fluxes in the upper troposphere. *J. Atmos. Sci.* **58**, 3019–3035.

DelSole, T. & Farrell, B. F. 1996 The quasi-linear equilibration of a thermally mantained stochastically excited jet in a quasigeostrophic model. *J. Atmos. Sci.* **53**, 1781–1797.

Dritchel, D. G. & McIntyre, M. E. 2008 Multiple jets as PV staircases: the Phillips effect and the resilience of eddy-transport barriers. *J. Atmos. Sci.* **65**, 855–874.

Farrell, B. F. & Ioannou, P. J. 1993 Stochastic dynamics of baroclinic waves. *J. Atmos. Sci.* **50**, 4044–4057.

Farrell, B. F. & Ioannou, P. J. 1994 A theory for the statistical equilibrium energy spectrum and heat flux produced by transient baroclinic waves. *J. Atmos. Sci.* **51**, 2685–2698.

Farrell, B. F. & Ioannou, P. J. 1995 Stochastic dynamics of the midlatitude atmospheric jet. *J. Atmos. Sci.* **52**, 1642–1656.

Farrell, B. F. & Ioannou, P. J. 1996 Generalized stability. Part I: Autonomous operators. *J. Atmos. Sci.* **53**, 2025–2040.

Farrell, B. F. & Ioannou, P. J. 2003 Structural stability of turbulent jets. *J. Atmos. Sci.* **60**, 2101–2118.

Farrell, B. F. & Ioannou, P. J. 2007 Structure and spacing of jets in barotropic turbulence. *J. Atmos. Sci.* **64**, 3652–3665.

Fjörtöft, R. 1953 On the changes in the spectral distribution of kinetic evergy for two-dimensional, non-divergent flow. *Tellus* **5**, 120–140.

Gill, A. E. 1974 The stability on planetary waves on an infinite beta-plane. *Geophys. Astrophys. Fluid Dyn.* **6**, 29–47.

Legras, B. & Ghil, M. 1985 Persistent anomalies, blocking and variations in atmospheric predictability. *J. Atmos. Sci.* **42**, 433–471.

Lilly, Douglas K. 1969 Numerical simulation of twodimensional turbulence. *Phys. Fluids* **12**, II240–II249.

Marston, J. B. 2012 Atmospheres as nonequilibrium condensed matter. *Annu. Rev. Condens.Matter Phys* **3**, 285–310.

Marston, J. B., Conover, E. & Schneider, T. 2008 Statistics of an unstable barotropic jet from a cumulant expansion. *J. Atmos. Sci.* **65**, 1955–1966.

Miller, J. 1990 Statistical mechanics of Euler equation in two-dimensions. *Phys. Rev. Lett.* **65**, 2137–2140.

O'Gorman, P. A. & Schneider, T. 2007 Recovery of atmospheric flow statistics in a general circulation model without nonlinear eddy-eddy interactions. *Geophys. Res. Lett.* **34**, L22801.

Rhines, P. B. 1975 Waves and turbulence on a beta-plane. *J. Fluid Mech.* **69**, 417–433.

Robert, R. & Sommeria, J. 1991 Statistical equilibrium states for two-dimensional flows. *J. Fluid Mech.* **229**, 291–310.

Schoeberl, M. R. & Lindzen, R. S. 1984 A numerical simulation of barotropic instability. Part I: Wave-mean flow interaction. *J. Atmos. Sci.* **41** (8), 1368–1379.

Srinivasan, K. & Young, W. R. 2012 Zonostrophic instability. *J. Atmos. Sci.* **69** (5), 1633–1656.

Vallis, G. K. & Maltrud, M. E. 1993 Generation of mean flows and jets on a beta plane and over topography. *J. Phys. Oceanogr.* **23**, 1346–1362.

Vasavada, A. R. & Showman, A. P. 2005 Jovian atmospheric dynamics: an update after Galileo and Cassini. *Rep. Prog. Phys.* **68**, 1935–1996.

Williams, G. P. 1978 Planetary circulations: 1. Barotropic representation of Jovian and terrestrial turbulence. *J. Atmos. Sci.* **35**, 1399–1426.

Zhang, Y. & Held, I. M. 1999 A linear stochastic model of a GCM's midlatitude storm tracks. *J. Atmos. Sci.* **56**, 3416–3435.

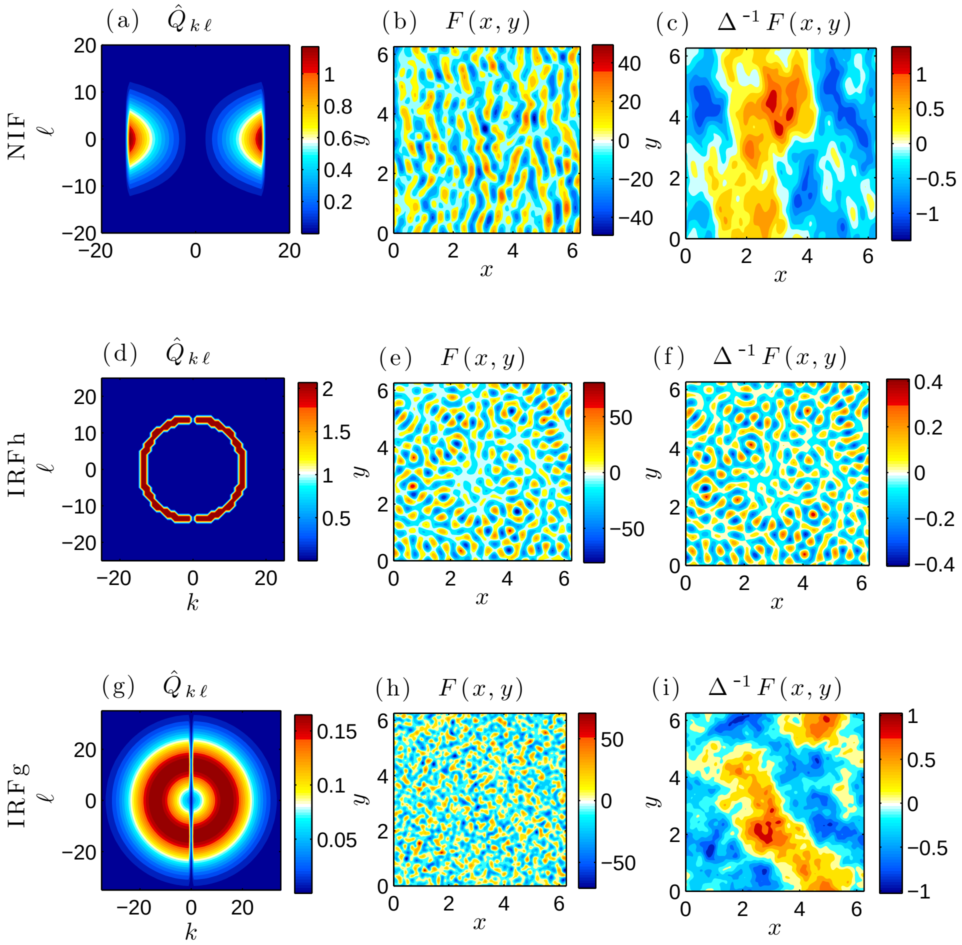

Figure 1. Stochastic forcing spatial wavenumber spectra and examples of realizations in physical variables. Shown for NIF with zonal wavenumbers $k = 1, \ldots, 14$ and $s = 0.2/\sqrt{2}$ are: (a) enstrophy spectrum, $\hat{Q}_{k\ell}$, (b) vorticity, (c) streamfunction. For IRFh at $K_f = 14$ and $\delta k_f = 1$: (d) enstrophy spectrum $\hat{Q}_{k\ell}$, (e) vorticity, (f) streamfunction. For IRFg at $K_f = 14$ and $\delta k_f = 8$: (g) enstrophy spectrum $\hat{Q}_{k\ell}$, (h) vorticity, (i) streamfunction.

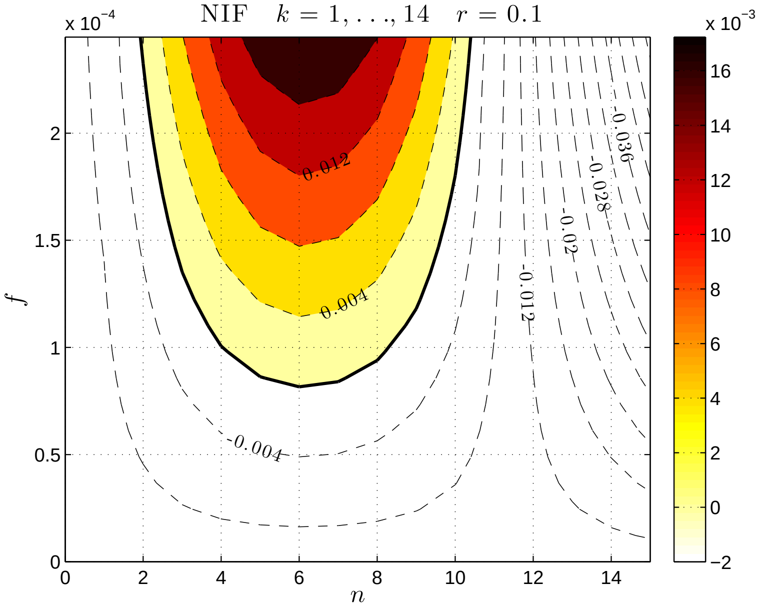

FIGURE 2. Growth rate, σ_r, of the SSST eigenfunction with jet structure $\delta U_n = \sin(ny)$ as a function of meridional wavenumber, n, and forcing amplitude, f, for NIF with $k = 1, \ldots, 14$. The stability boundary ($\sigma_r = 0$) is marked with thick solid line and the unstable region is shaded. The least forcing required for instability, $f_c = 8.16 \times 10^{-5}$, occurs at $n = 6$. Other parameters are: $r = 0.1$, $r_{\mathrm{m}} = 0.01$, $\beta = 10$.

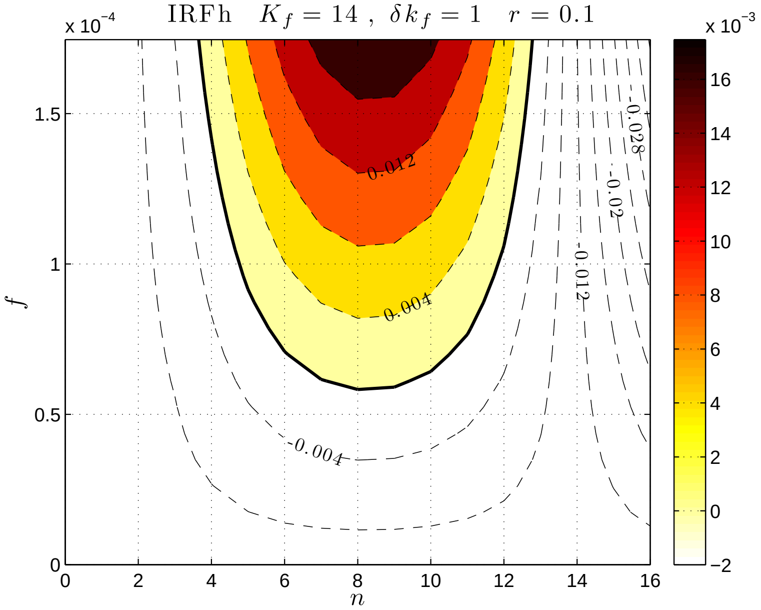

FIGURE 3. Growth rate, σ_r, of the SSST eigenfunction with jet structure $\delta U_n = \sin(ny)$ as a function of meridional wavenumber, n, and forcing amplitude, f, for IRFh at $K_f = 14$ with $\delta k_f = 1$. The stability boundary ($\sigma_r = 0$) is marked with thick solid line and the unstable region is shaded. The least required for instability, $f_c = 5.82 \times 10^{-5}$, occurs at $n = 8$. Other parameters are: $r = 0.1$, $r_{\mathrm{m}} = 0.01$, $\beta = 10$.

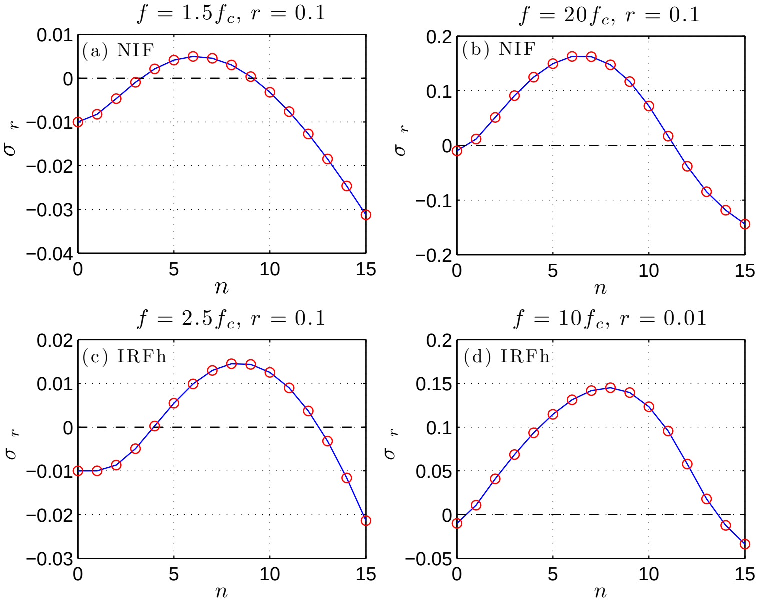

FIGURE 4. Growth rate, σ_r, of the SSST eigenfunction with jet structure $\delta U_n = \sin(ny)$ as a function of jet meridional wavenumber, n. For NIF with $k = 1, \dots, 14$ shown are the growth rates for (a) $f = 1.5 f_c$ and $r = 0.1$, (b) for $f = 20 f_c$ and $r = 0.1$. For IRFh at $K_f = 14$ with $\delta k_f = 1$ shown are: (c) the growth rates for $f = 2.5 f_c$ and $r = 0.1$, (d) for $f = 10 f_c$ and $r = 0.01$. Other parameters are: $r_{\mathrm{m}} = 0.01$, $\beta = 10$.

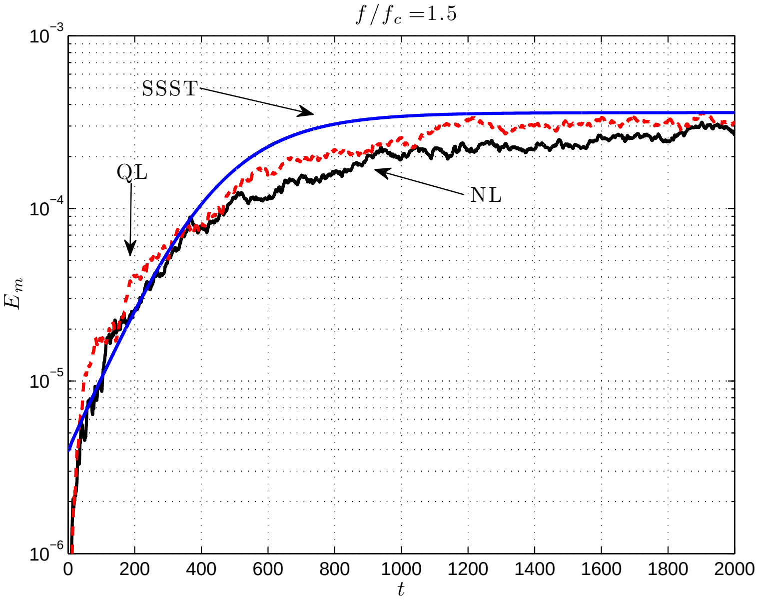

FIGURE 5. Development of mean flow energy, E_m, for NL and QL simulations starting from a state of rest with NIF at $k = 1, \ldots, 14$ and $f = 1.5 f_c$. Also shown is the exponential growth and subsequent equilibration of E_m under SSST dynamics with initial condition the most unstable SSST eigenfunction. This figure demonstrates that SSST dynamics accurately predicts nonlinear jet equilibration at finite amplitude as well as the initial instability and exponential growth of the jets. Parameters are $\beta = 10$, $r = 0.1$, $r_{\rm m} = 0.01$.

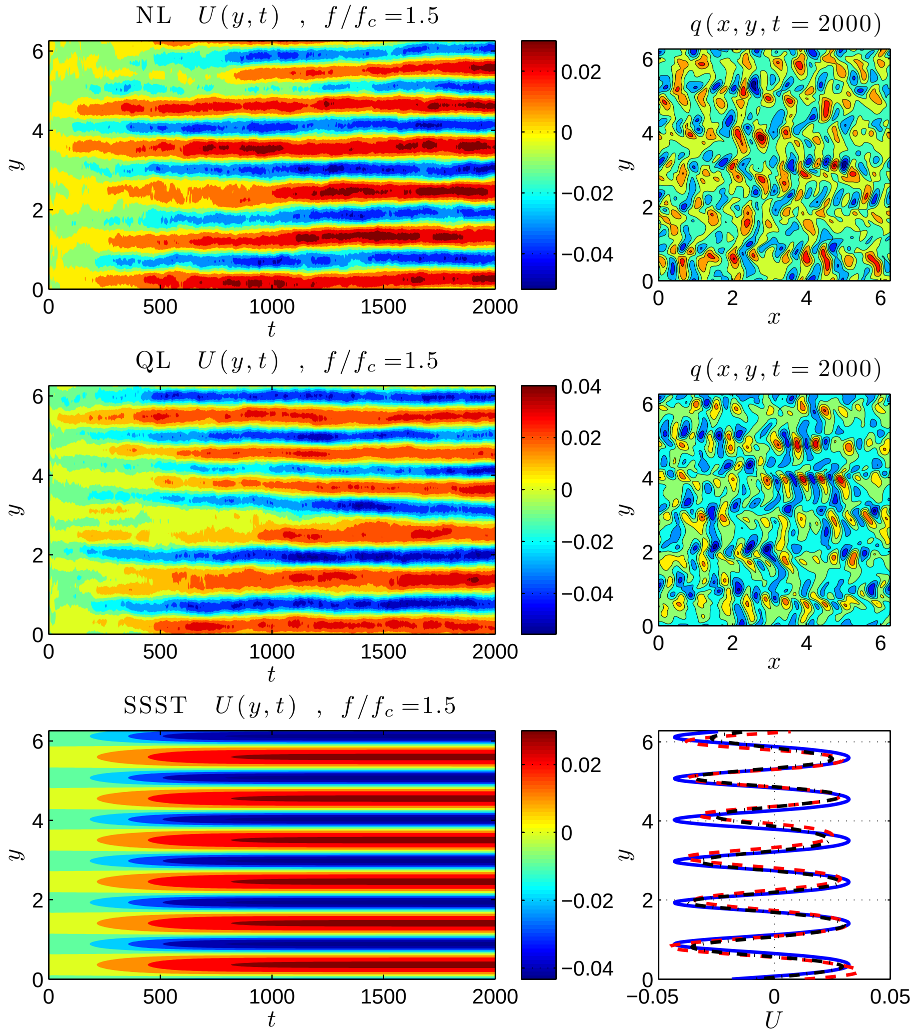

FIGURE 6. Hovmöller diagrams of jet emergence in the NL, QL and SSST simulations shown in figure 5. Shown for the NL, QL and SSST simulations are $U(y,t)$ (left panels) and for the NL and QL simulations the vorticity fields at $t = 2000$ (top and middle right panels). Also shown are the equilibrium jets in the NL (dash-dot-black), QL (dashed - red), and SSST (solid - blue) simulation (bottom right panel). This figure shows that SSST predicts the structure, growth and equilibration of weakly forced jets in both the QL and NL simulations (cf. figure 4a).

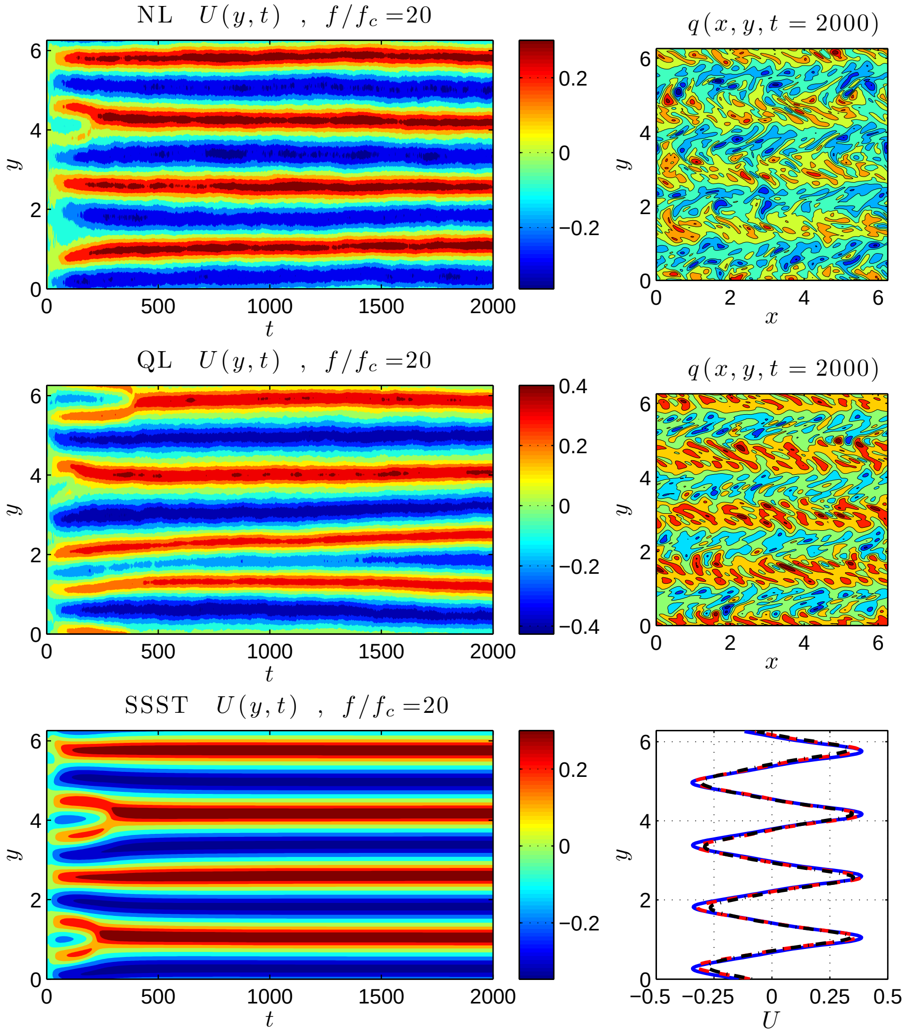

FIGURE 7. Hovmöller diagrams of jet emergence in NL, QL and SSST simulations with NIF forcing of $k = 1, \ldots, 14$ with $f = 20f_c$. Shown for the NL, QL and SSST simulations are $U(y,t)$ (left panels) and for the NL and QL simulations the vorticity fields at $t = 2000$ (top and middle right panels). Also shown are the equilibrium jets in the NL (dash-dot-black), QL (dashed - red), and SSST (solid - blue) simulation (bottom right panel). This figure shows that SSST predicts the structure, growth and equilibration of immoderately forced jets in both the QL and NL simulations (cf. figure 4b). Parameters are $r = 0.1$, $r_{\rm m} = 0.01$ and $\beta = 10$.

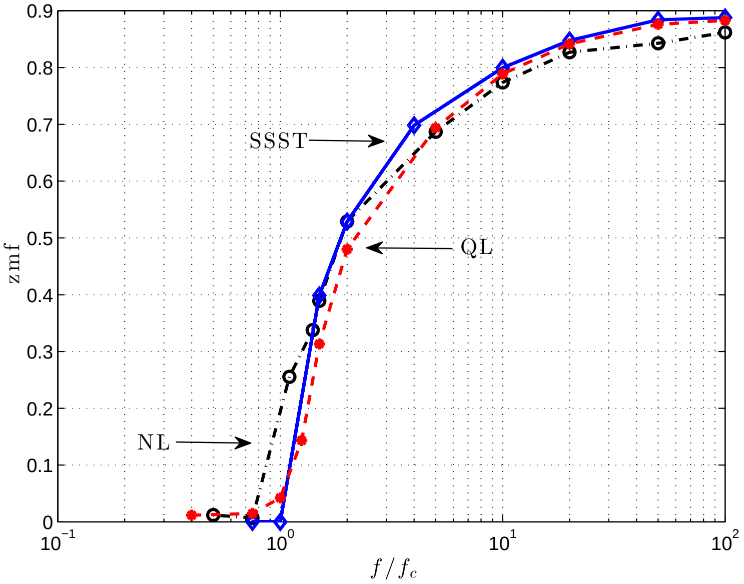

FIGURE 8. Bifurcation structure comparison for jet formation in SSST, QL, and NL. Shown is the zmf index of jet equilibria for NIF at $k = 1, \ldots, 14$ as a function of the forcing amplitude f/f_c for the NL simulation (dash-dot and circles), the QL simulation (dashed and dots) and the SSST (solid and diamonds). Parameters are $\beta = 10$, $r = 0.1$, $r_{\mathrm{m}} = 0.01$.

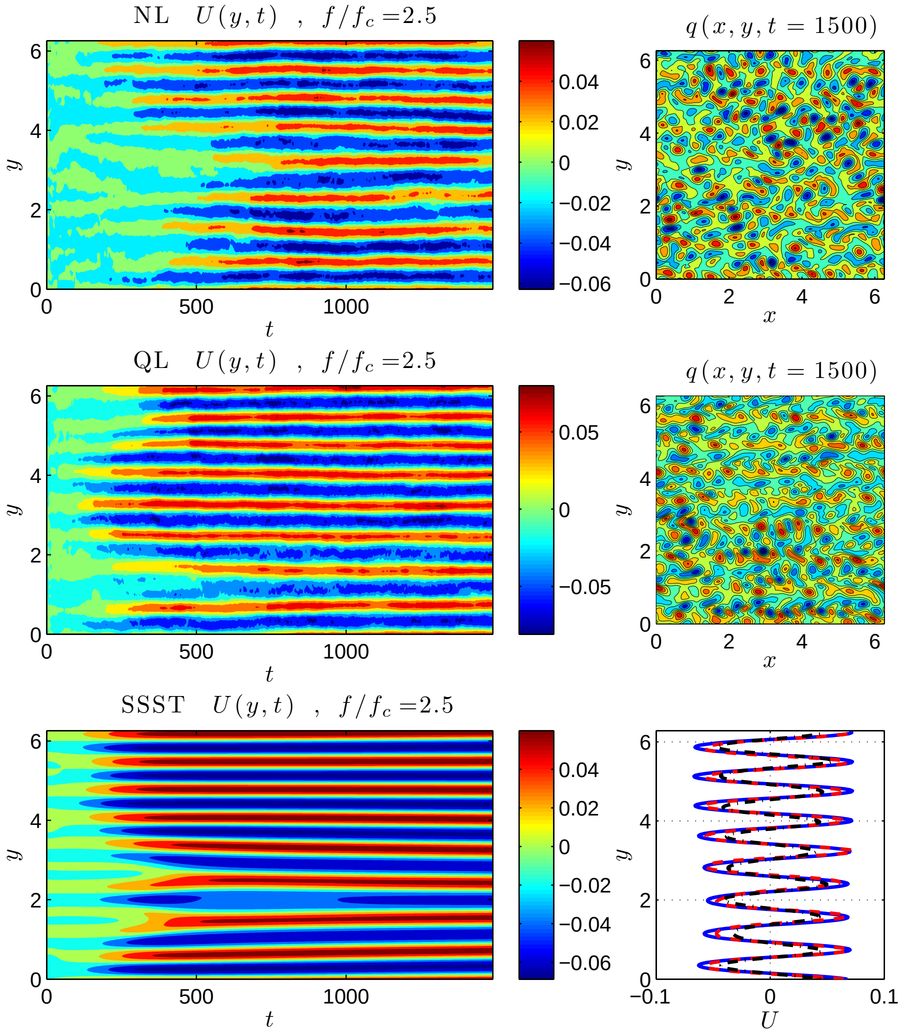

FIGURE 9. Hovmöller diagrams of jet emergence in NL, QL and SSST simulations with IRFh forcing at $f = 2.5f_c$ and with $K_f = 14$, $\delta k_f = 1$. Shown for the NL, QL and SSST simulations are $U(y,t)$ (left panels) and for the NL and QL simulations the vorticity fields at $t = 1500$ (top and middle right panels). Also shown are the equilibrium jets in the NL (dash-dot-black), QL (dashed - red), and SSST (solid - blue) simulation (bottom right panel). This figure shows that SSST predicts the structure, growth and equilibration of jets obtained in both the QL and NL simulations (cf. figure 4c). Parameters are $r = 0.1$, $r_{\mathrm{m}} = 0.01$ and $\beta = 10$.

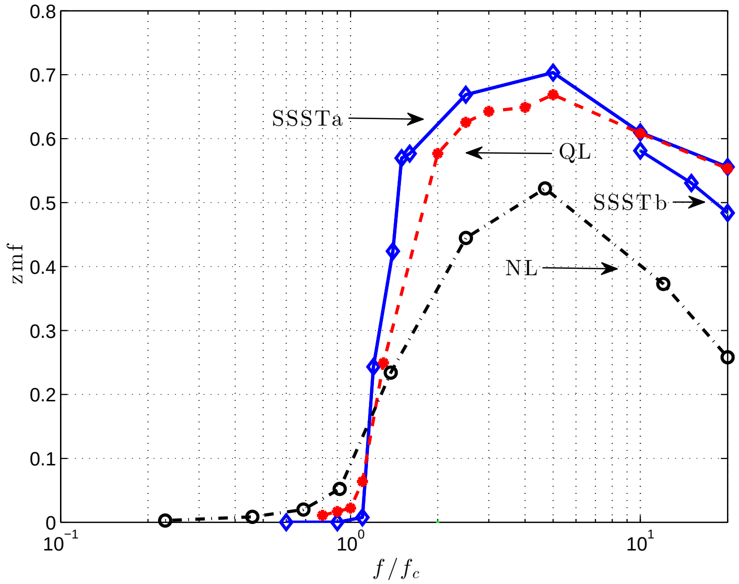

FIGURE 10. Bifurcation structure comparison for jet formation in SSST, QL, and NL. Shown is the zmf index of jet equilibria for IRFh with $K_f = 14$ and $\delta k_f = 1$ as a function of the forcing amplitude f/f_c for the NL simulation (dash-dot and circles), the QL simulation (dashed and dots) and the SSST (solid and diamonds) for IRFh (SSSTa), as well as the SSST for the equivalent spectrum to that obtained in NL as a consequence of modification of the IRFh spectrum by the nonlinear cascade (SSSTb) with forcing amplitude $f = 20f_c$. This figure shows that the bifurcation to jet formation in NL and QL simulations is captured by SSST and that SSST overestimates the NL jet amplitude when the forcing is high, even when account is taken for the nonlinear modification of the spectrum. Parameters are $\beta = 10$, $r = 0.1$, $r_{\mathrm{m}} = 0.01$.

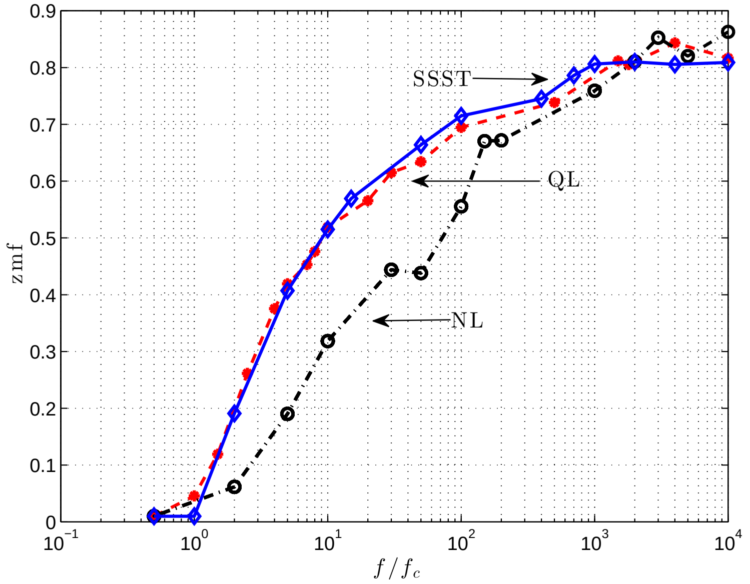

FIGURE 11. Bifurcation structure comparison for jet formation in SSST, QL, and NL. Shown is the zmf index of jet equilibria for IRFg with $K_f = 14$ and $\delta k_f = 8$ as a function of the forcing amplitude f/f_c for the NL simulation (dash-dot and circles), the QL simulation (dashed and dots) and the SSST (solid and diamonds). Parameters are $\beta = 10$, $r = 0.1$, $r_{\mathrm{m}} = 0.01$.

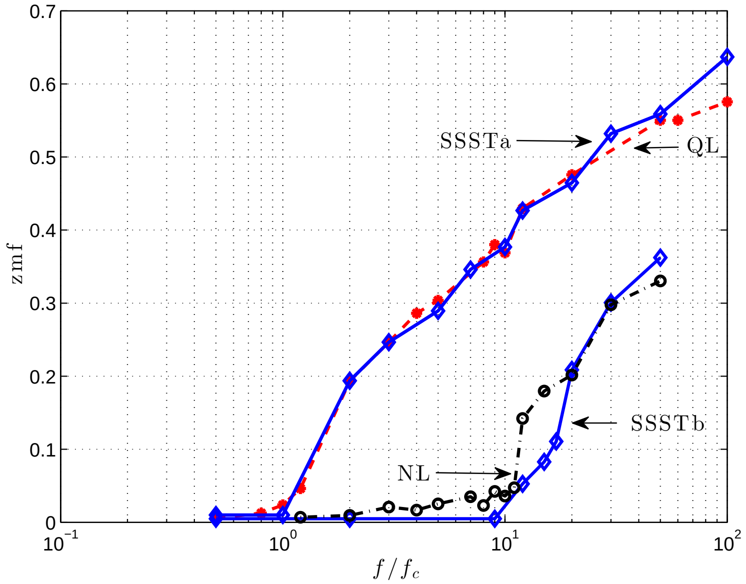

FIGURE 12. Bifurcation structure comparison for jet formation in SSST, QL, and NL. Shown is the zmf index of jet equilibria for NIF at $k = 1, \ldots, 14$ as a function of the forcing amplitude f/f_c for the NL simulation (dash-dot and circles), the QL simulation (dashed and dots) and the SSST NIF (SSSTa), as well as the SSST for the equivalent spectrum to that obtained in NL as a consequence of modification of the NIF spectrum by the nonlinear cascade (SSSTb). The bifurcation in the NL simulations occurs at $f_c^{(\mathrm{NL})} \approx 11 f_c$. This figure shows that the structure of the jet in NL simulations is captured by the SSST if account is taken of the nonlinear modification of the spectrum. Parameters are $\beta = 10$, $r = 0.01$, $r_{\mathrm{m}} = 0.01$.

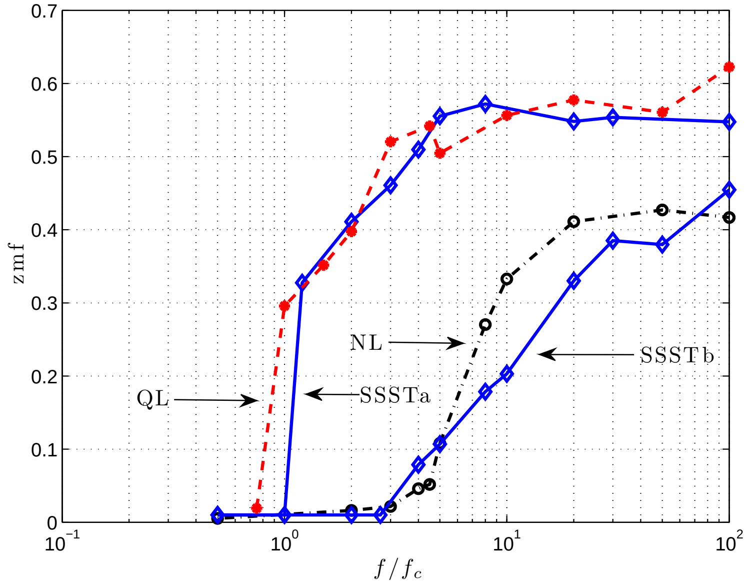

FIGURE 13. Bifurcation structure comparison for jet formation in SSST, QL, and NL. Shown is the zmf index of jet equilibria for IRFh at $K_f = 14$ with $\delta k_f = 1$ as a function of the forcing amplitude f/f_c for the NL simulation (dash-dot and circles), the QL simulation (dashed and dots) and the SSST IRFh (SSSTa), as well as the SSST for the equivalent spectrum to that obtained in NL as a consequence of modification of the IRFh spectrum by the nonlinear cascade (SSSTb). The bifurcation in the NL simulations occurs at $f_c^{(\mathrm{NL})} \approx 4 f_c$. This figure shows that the structure of the jet in NL simulations is captured by the SSST if account is taken of the nonlinear modification of the spectrum. Parameters are $\beta = 10$, $r = 0.01$, $r_{\mathrm{m}} = 0.01$.

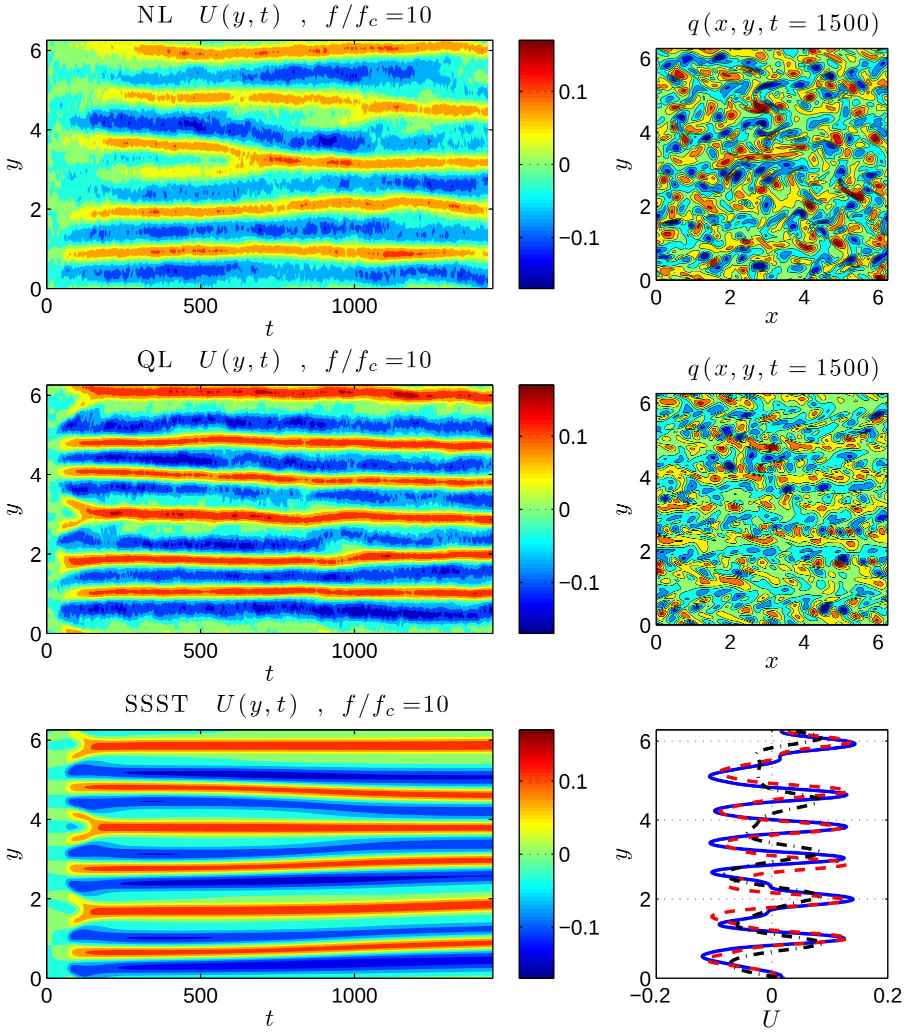

FIGURE 14. Hovmöller diagrams of jet emergence in NL, QL and SSST simulations with IRFh forcing at $f = 10f_c$ and with $K_f = 14$, $\delta k_f = 1$. Shown for the NL, QL and SSST simulations are $U(y,t)$ (left panels) and for the NL and QL simulations the vorticity fields at $t = 1500$ (top and middle right panels). Also shown are the equilibrium jets in the NL (dash-dot-black), QL (dashed - red), and SSST (solid - blue) simulation (bottom right panel). This figure shows that SSST predicts the structure, growth and equilibration of jets obtained in both the QL and NL simulations (cf. figure 4d). The jet maintained in the NL simulation has an amplitude which is 10% less than the amplitude of the jet of the QL simulation. Parameters are $\beta = 10$, $r = 0.01$, $r_{\mathrm{m}} = 0.01$.

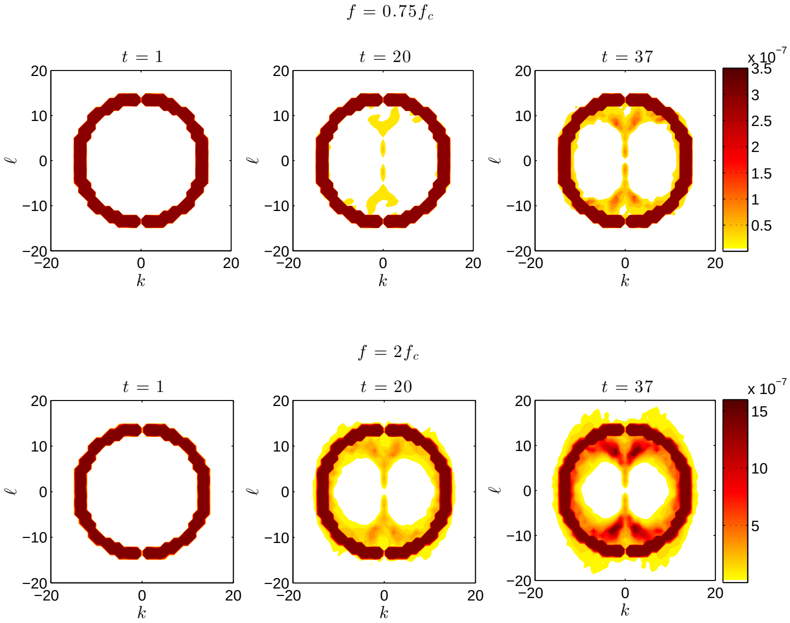

FIGURE 15. Evolution toward equilibrium of the energy spectrum, $E_{k\ell} = \frac{1}{2}\ |\hat{q}_{k\ell}|^2/(k^2 + \ell^2)$, in NL under IRFh forcing with $K_f = 14$ and $\delta k_f = 1$. At $t = 0$ the spectrum is that of the homogeneous SSST equilibrium. Top panels: The spectrum at $t = 1,\ 20,\ 37$ for $f = 0.75 f_c$. Bottom panels: The spectrum at $t = 1,\ 20,\ 37$ for $f = 2 f_c$. The upscale energy cascade produces the familiar dumbbell spectrum. The distortion of the spectrum increases with f. The parameters are $r = 0.01$, $r_{\rm m} = 0.01$ and $\beta = 10$.

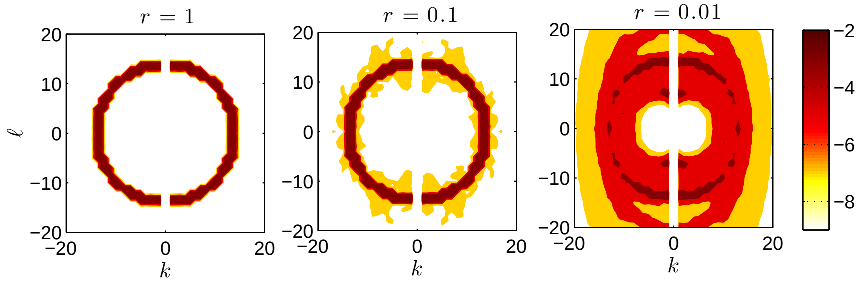

FIGURE 16. Equilibrium enstrophy spectrum, $\log\left(2r|\hat{q}_{k\ell}|^2\right)$, of NL simulations, in which perturbation-perturbation interactions are included but the $k = 0$ component is excluded for various damping rates. The example is for IRFh forcing at $f = 2f_c$ and with $K_f = 14$, $\delta k_f = 1$. Shown is the spectrum: (a) for linear damping coefficient $r = 1$ (left panel), (b) $r = 0.1$ (middle panel) and $r = 0.01$ (right panel). The critical, f_c, is a function of r and is obtained from SSST. All spectra have been normalized by their maximum value. This figure shows that for relatively small damping the perturbation spectra in NL simulations are close to the SSST perturbation spectra while for weak damping the equilibrium spectrum in NL differs substantially from that in SSST. Other parameters are $\beta = 10$ and $r_{\mathrm{m}} = 0.01$.

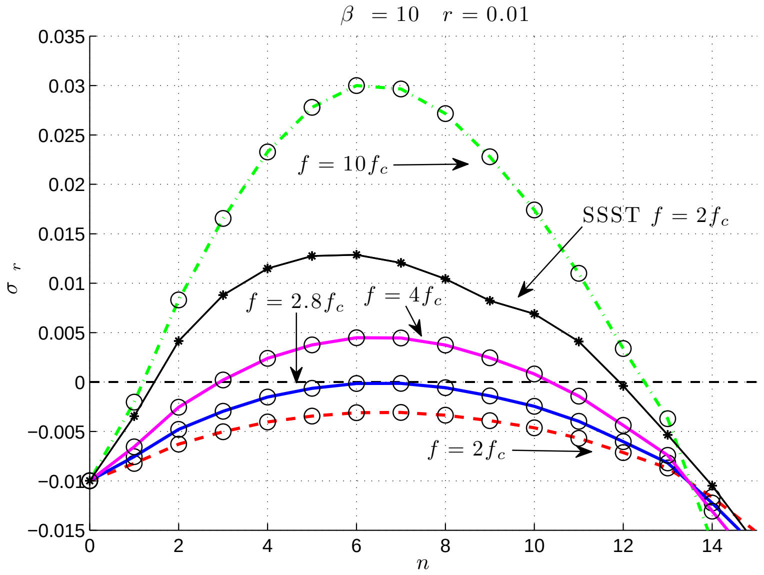

FIGURE 17. SSST jet instability growth rates for the equilibrium spectrum obtained in the NL dynamics subjected to IRFh forcing at $K_f = 14$, $\delta k_f = 1$ for $r = 0.01$ (shown in the right panel of figure 16). Shown are the growth rates, σ_r, as a function of the meridional wavenumber, n, with forcing amplitude $f = 2f_c$, $f = 2.8f_c$, $f = 4f_c$ and $f = 10f_c$. Also shown are the growth rates for the SSST equilibrium with IRFh forcing at $f = 2f_c$ (solid-star line). This figure shows that the nonlinear interactions have modified the original ring spectrum making it more stable so that the modified flow state becomes unstable at $f = 2.8f_c$ and $n = 6$. With this modification, the NL simulations agree with the predictions of the SSST analysis as shown in figure 13. Other parameters are $\beta = 10$ and $r_{\mathrm{m}} = 0.01$.

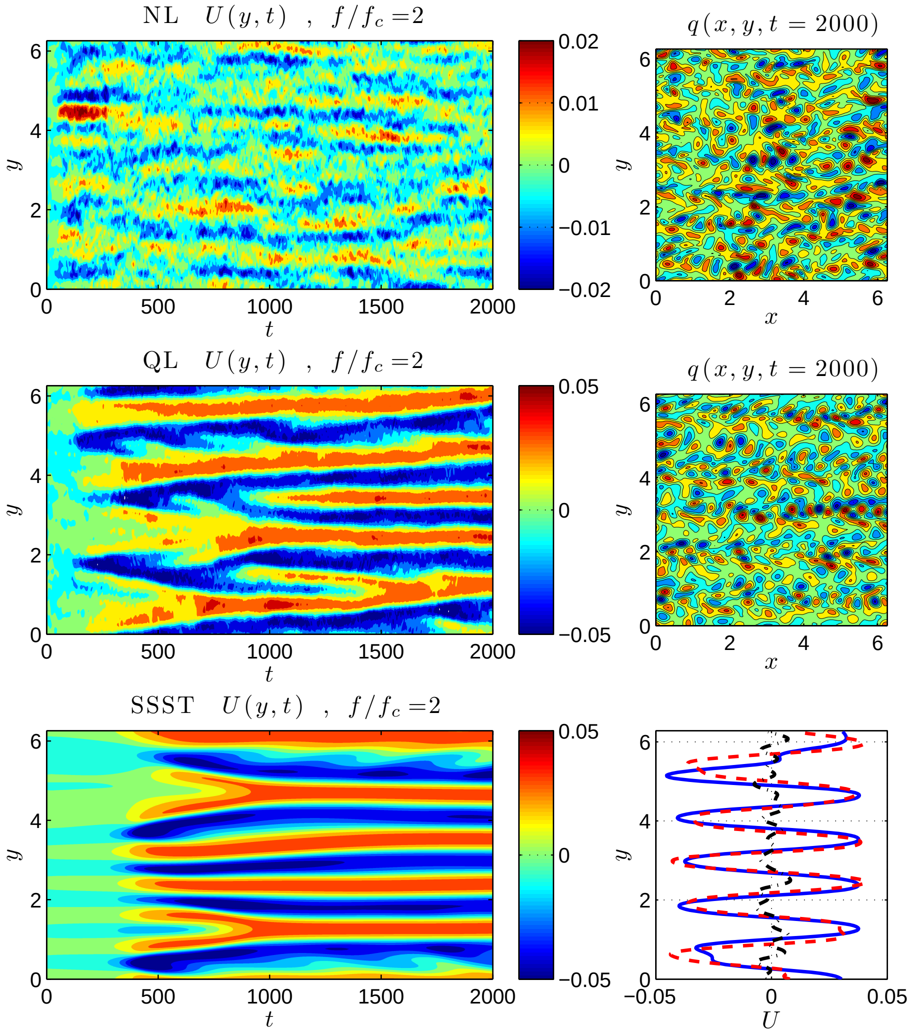

FIGURE 18. Hovmöller diagrams of jet emergence in NL, QL and SSST simulations with IRFh forcing at $f = 2f_c$ and with $K_f = 14$, $\delta k_f = 1$. Shown for the NL, QL and SSST simulations are $U(y,t)$ (left panels) and for the NL and QL simulations the vorticity fields at $t = 2000$ (top and middle right panels). Also shown are the equilibrium jets in the NL (dash-dot-black), QL (dashed - red), and SSST (solid - blue) simulation (bottom right panel). At $f = 2f_c$ the NL simulation is subcritical but the $n = 6$ structure of the least stable SSST mode is discernible (cf. figure 16). This figure shows that stable SSST eigenmodes can be excited by fluctuations in NL simulations in the subcritical regime. Parameters are $\beta = 10$, $r = 0.01$, $r_{\mathrm{m}} = 0.01$.

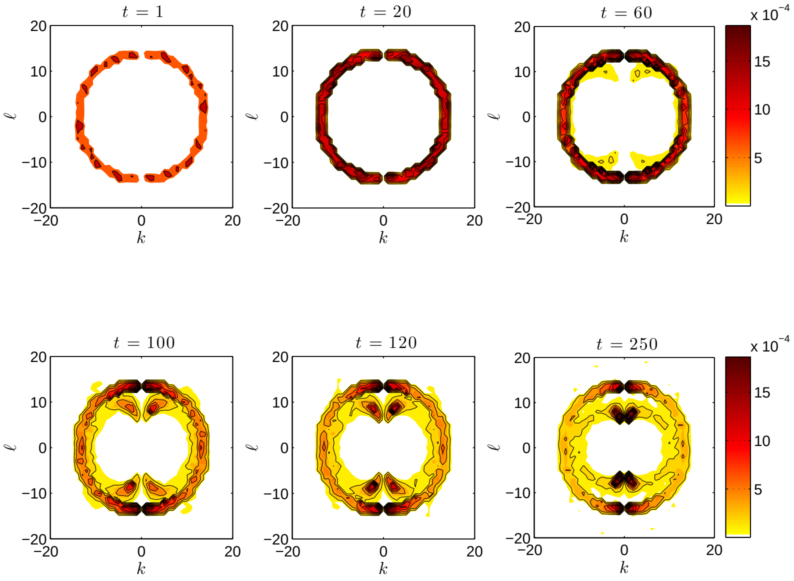

FIGURE 19. Evolution of the ensemble average enstrophy spectrum, $|\hat{q}_{k\ell}|^2$, for a set of NL simulations with isotropic ring forcing at wavenumber $K_f = 14$, $\delta k_f = 1$, and forcing amplitude $f = 2f_c$. Parameters are $\beta = 10$, $r = 0.01$, $r_\mathrm{m} = 0.01$.

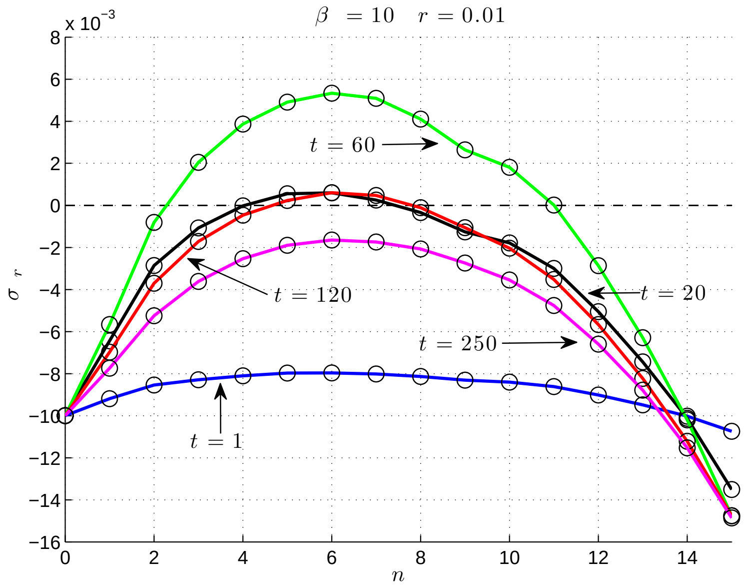

FIGURE 20. Instantaneous SSST growth rates, σ_r, as a function of jet meridional wavenumber, n, for equilibria with the enstrophy spectra shown in figure 19. The spectrum of the evolving NL simulation becomes SSST unstable at $t \approx 20$ and stabilizes again at $t \approx 120$. Parameters are $\beta = 10$, $r = 0.01$, $r_{\mathrm{m}} = 0.01$.

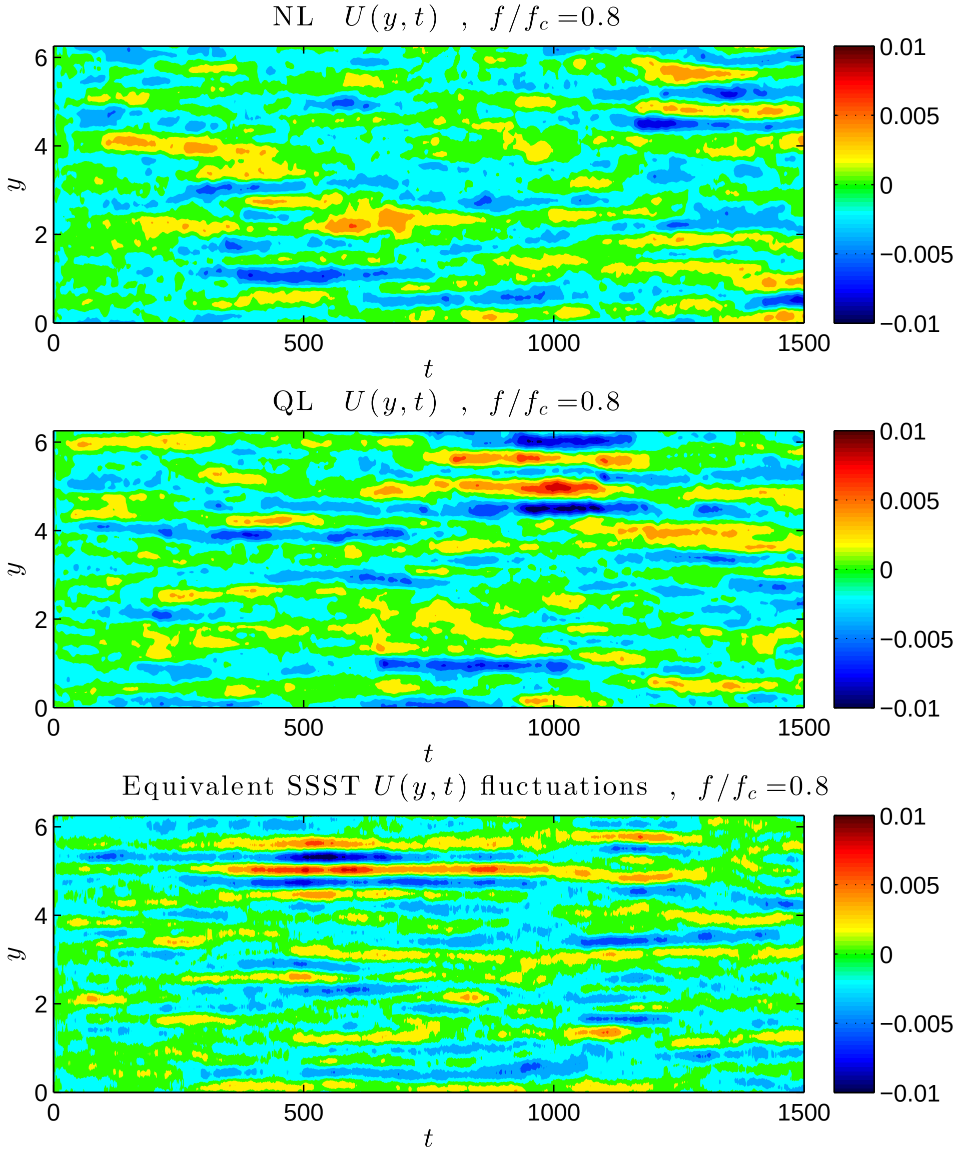

FIGURE 21. Hovmöller diagrams of intermittent jet structure in NL and QL simulations at subcritical forcing $f = 0.8 f_c$. Shown are $U(y,t)$ resulting for: NL (top) and QL (middle) simulations and the $U(y,t)$ that results from random excitation of the SSST damped modes (bottom panel). These plots were obtained using IRFh forcing with $K_f = 14$, $\delta k_f = 1$ and $r = 0.1$ (cf. figure 10). This figure shows that the manifold of SSST damped modes are revealed by being excited in the fluctuating NL and QL simulations. Other parameters are $\beta = 10$, $r_{\mathrm{m}} = 0.01$.

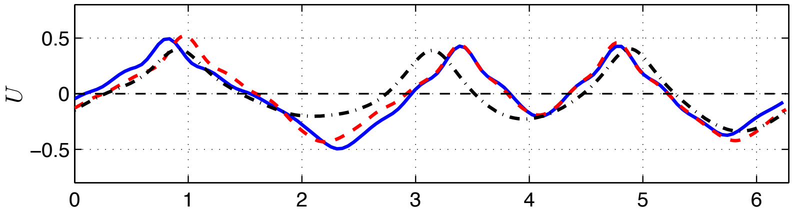

FIGURE 22. The mean jet structure, $U(y)$, for NL (dash-dot), QL (dashed) and SSST (solid) simulations for IRFh at $K_f = 14$ with $\delta k_f = 1$ for $f = 100 f_c$ and perturbation damping $r = 0.01$. There is good agreement between the jet structure in the NL simulation and the jets obtained with QL and SSST, despite the difference in the zmf index (cf. figure 13). The other parameters are $\beta = 10$, $r_{\mathrm{m}} = 0.01$.

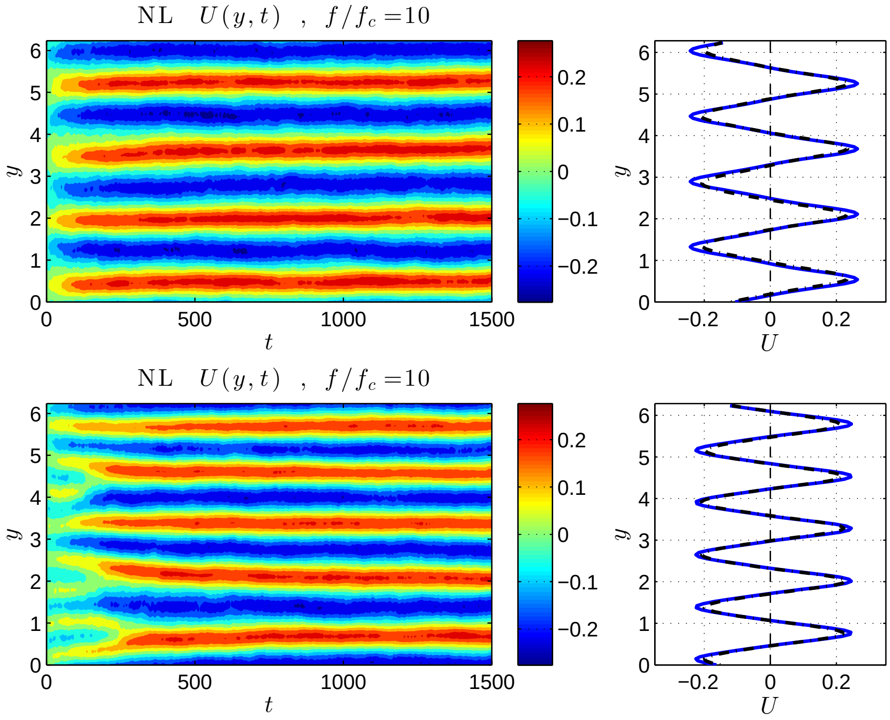

FIGURE 23. Reflections in NL simulations of multiple equilibria predicted by SSST. Left panels: Hovmöller diagrams of NL simulations showing the equilibrium with 4 jets (top) and with 5 jets (bottom). Right panels: comparison of the SSST equilibrium jets (solid) with the average jets obtained from the NL simulation (dashed). Parameters: NIF forcing at $k = 1, \ldots, 14$ with amplitude $f = 10f_c$, $\beta = 10$, $r = r_m = 0.1$.